Master's thesis

NTNU
Norwegian University of Science and Technology
Faculty of Natural Sciences
Department of Physics

Sara Gasparini

Statistical properties of backscatter from the Longyearbyen SuperDARN radar

Master's thesis in Physics
Supervisor: Prof. Patrick Espy
Co-supervisor: Dr. Emma Bland, UNIS
August 2019

NTNU
Norwegian University of
Science and Technology

NTNU
Norwegian University of
Science and Technology

Statistical properties of backscatter from the Longyearbyen SuperDARN radar

Sara Gasparini

MSc in Physics
Submission date: August 2019
Supervisor: Prof. Patrick Espy
Co-supervisor: Dr. Emma Bland, UNIS

Norwegian University of Science and Technology
Department of Physics

"I would rather have questions that can't be answered than answers that can't be questioned."

— Richard P. Feynman

Acknowledgements

To my UNIS supervisor, Dr. Emma Bland: thank you for supporting me since from the very beginning guiding me through coding and enlightening scientific discussions. Moreover, thank you for providing me always with detailed feedback on the research throughout the year, and the thesis drafts. Most of all, thank you for believing in my capabilities as a scientist and for encouraging me to continue the academic career. I will always be grateful for what I have learn from you during this year.

To my NTNU supervisor, Prof. Patrick Espy: thank you for giving me the chance to write my Master thesis in Svalbard and for being of help every time it was needed.

To my boyfriend, Simon: thank you for all the physics discussions, even if sometimes they drive us nuts, and for assisting me a lot with the last part of the thesis and hearing me talking about nothing but SuperDARN and polar cap patches. Thank you for all your emotional support that I receive from you every day. I am so much looking forward to be doing more physics together and finally do our Parker model.

To my family, mum and dad, Rachele, grandmother and grandfather and Maurizio: thank you for all your support. You are always there by my side even if so far away. Thank you Rachele for your graphic skills. Thank you grandma and granddad for the many letters and postcards during this year and thank you auntie Elena for all your special support with the box of food. This made me feel at home at times.

To the UNIS Geophysics Department: thank you for welcoming me in the group and be such a great company throughout the year.

To Svalbard, a special place: thank you for giving me the chance to meet Simon and for all you have done to give me life skills and teaching me how to be an adult.

Abstract

The Super Dual Auroral Radar Network (SuperDARN) has been a useful tool to study the mid-latitude and high-latitude ionospheres for more than 20 years. The new SuperDARN radar on Svalbard (LYR) began operating in October 2016. This thesis presents the first statistical analysis of the backscatter detected by this radar over a full calendar year.

It is found that the LYR SuperDARN radar routinely detects backscatter from the E- and F- ionospheric layers, and also from the D-layer during periods of high-energy particle precipitation. Strong seasonal variations in backscatter occurrence are observed. In the F-layer, the echo occurrence reaches a maximum in the winter and a minimum in the summer. In contrast, the E-layer echo occurrence is greatest in the summer and lowest in the winter.

In addition to the echo occurrence, the average behaviour of the velocity and spectral width parameters measured by the radar are investigated. A key feature of the data is cusp signatures for the summer months, which are identified by enhanced spectral widths. In the winter, high spectral widths and high velocities are measured within the entire dayside auroral oval between 6–18 MLT. Ionospheric convection patterns for the dayside sector are found to have a seasonal behaviour and a strong dependence on the B_y and B_z components of the interplanetary magnetic field.

Finally, preliminary evidence of polar cap patches detectable with the LYR SuperDARN radar is presented. Polar cap patches are a good scattering target due to their high electron densities and this highlights an opportunity to study the polar ionospheric convection using the Svalbard SuperDARN radar.

Table of Contents

Chapter 1

Introduction

This thesis is about the study of the backscatter from the Longyearbyen (LYR) Super Dual Auroral Radar (SuperDARN) radar. This high frequency (HF) radar is part of a network of more than 30 radars and it has been operational since October 2016. For the first time a statistical analysis is done for year 2017.

The LYR observes a portion of the northern polar ionosphere, which is defined as the ionospheric region above the Arctic Circle, above 66° geographic latitude. The high latitude ionosphere is very different from the mid-latitude and the low-latitude ionosphere. This is because the variable solar wind has a strong influence on the dynamics of the polar ionosphere and drives processes such as particle precipitation events in the form of substorms or day-side reconnection. Moreover, solar energetic particles are a source of additional ionisation giving complexity to the ionospheric radio propagation particularly in this region [*Hunsucker and Hargreaves*, 2007].

In this chapter an introductory journey from the Sun to the Earth system is made to introduce the fundamental processes that lead to the features investigated in this thesis.

1.1 The Sun

The Sun is the star that affects the planets in the solar system and the Earth's environment. Kristian O. B. Birkeland (1867-1917) was one of the first scientists to hypothesize a relationship between the Sun and the Earth's system. He showed, with the terrella experiment, that the formation of the auroral oval is caused by the geomagnetic field and a hypothetical continuous stream of energetic particles [*Birkeland*, 1908]. Later on, S. Chapman and V. Ferraro established the concept of plasma flow from the Sun [*Chapman and Ferraro*, 1931].

The Sun is a cold magnetic star, classified as a yellow dwarf, that formed about 4.55×10^9 years ago from an interstellar cloud of gas. The Sun's mass is 1.99×10^{30} kg and it has an effective black body temperature of 5778 K. The star is composed of 92% hydrogen, the fuel for the nuclear reaction, and 8% helium, both primordial and as a waste product of the nuclear reaction. The solar structure is defined by six regions and they are illustrated in Fig. 1.1.

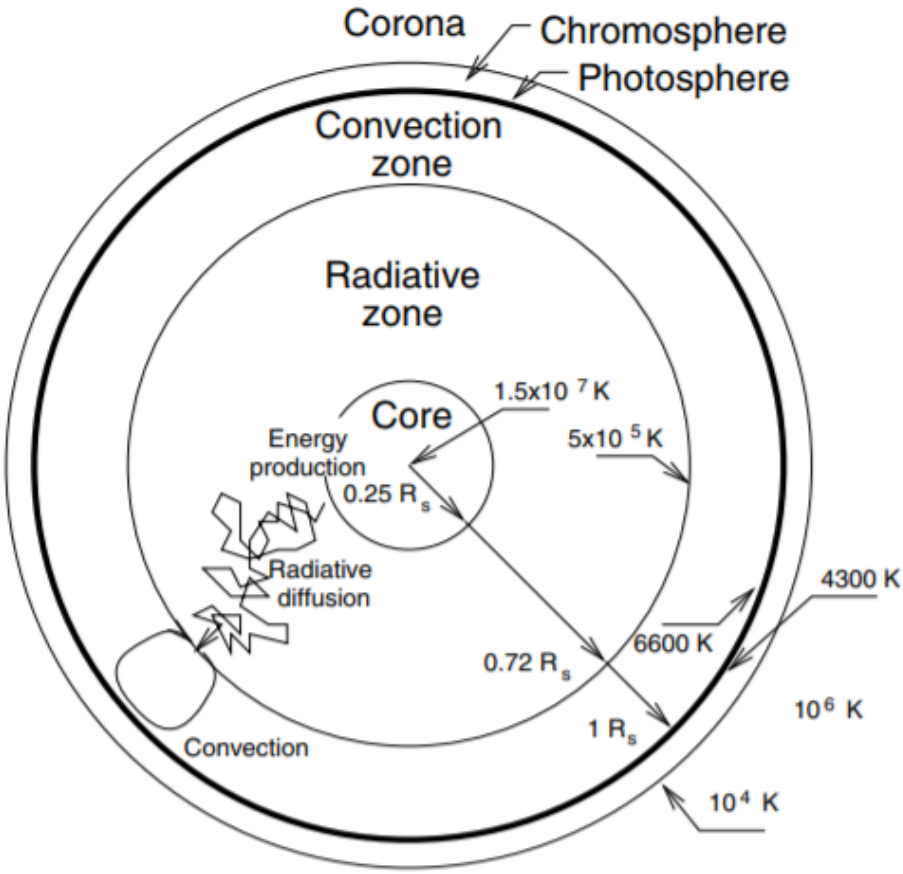

Figure 1.1: The structure of the Sun. From Koskinen [2011].

The core is the place where the nuclear fusion occurs and hydrogen is converted into helium. Moving outwards from the core, one encounters the radiative zone, where energy is transported by radiation, and then the convection zone, where energy is transported by convection through convection cells. Convection cells are visible as granulations in the photosphere. The photosphere is the top of the convection zone and, due to its optical thickness, prevents electromagnetic radiation from being detected. Above the stratosphere are the chromosphere and the solar corona, regions where the solar wind is likely to be accelerated [*Feldman et al.*, 2005; *Kallenrode*, 2013].

*L*YR backscatter properties

The temperature of the Sun varies while moving through the different regions; the core is the hottest place with temperatures of 15 million K. Going radially outward from the core, the temperature is steadily decreasing until the lower boundary of the chromosphere where the temperature starts increasing again reaching 2 million K in the corona [*Kallenrode*, 2013].

1.2 The solar wind

The solar atmosphere during solar minimum consists of coronal holes (CH) and quiet regions. In this period of the solar cycle, coronal holes are primarily located in the polar regions of the Sun and are associated with open magnetic field lines. Quiet regions, during solar minimum, cover the rest of the surface area and are associated with closed magnetic field lines [*Feldman et al.*, 2005; *Lowder et al.*, 2017]. Both active and quiet regions are responsible for the acceleration of the solar wind.

There are two types of solar wind during solar minimum: a slow component of about 350 km s^{-1} originating at mid-latitudes, surrounding the streamer belts in the corona, and a fast component of around 750 km s^{-1} streaming from both high heliographic latitudes and quiet regions of the Sun (QS) [*Feldman et al.*, 2005; *Koskinen*, 2011]. The solar wind is a plasma, a quasi- neutral ionized gas, composed of approximately 95% protons, 4% alpha particles (ionised helium He^{++}) and 1% minor species such as carbon, nitrogen, oxygen, neon, magnesium, silicon, manganese and iron [*Ogilvie and Coplan*, 1995]. However, there are strong differences between the elemental composition of slow and fast solar wind within the minor species. The slow solar wind is denser than the fast solar wind with a number density of about 1×10^7 m^{-3} at 1 AU whereas the fast solar wind has a number density of about 3×10^6 m^{-3}. The electron temperatures are also different for the two types of wind: about 1×10^3 K for the slow solar wind and around 1×10^5 K for the fast solar wind [*Zurbuchen et al.*, 2002].

1.3 The interplanary magnetic field (IMF)

The interplanetary magnetic field (IMF) is the Sun's magnetic field dragged into interplanetary space by the solar wind due to the frozen-in effect [*Yermolaev and Yermolaev*, 2010], described in the next section. This results in the behaviours of the IMF, such as orientation and motion, being driven by the solar wind [*Schwenn*, 2001].

The IMF can change in terms of overall magnitude and orientation. The magnitude is strongly influenced by the solar activity (in general, greater magnitude at greater activity), while the orientation is more influenced by the dynamics of the solar wind. The IMF can be broken down into three components: B_x, B_y and B_z. The coordinate system typically used when describing the IMF behaviour is the Geocentric Solar Ecliptic (GSE) coordinate system [*Hapgood*, 1992]. In this coordinate system the x axis is pointing from the Earth to the Sun, the y axis is pointing towards dusk in the ecliptic plane and the z axis is perpendicular to the ecliptic plane. The ecliptic plane is the plane of the Earth's orbit around the Sun.

B_z is particularly important when discussing space weather. Negative B_z, corresponding to southward IMF, can cause reconnection of the IMF with the Earth's magnetosphere leading to a strong influence on the Earth's plasma environment, whereas northward IMF reconnection processes occur less predictably and with smaller effects on the Earth's plasma environment.

1.3.1 Frozen-in concept

The frozen-in concept is the idea that the plasma and the magnetic field move together with relatively little individual motion. The concept originates through an equation encountered in magneto-hydrodynamics (MHD) theory. Equation 1.1 is the induction equation, which is derived using generalised Ohm's law, Faraday's law and Ampère's law. The induction equation describes the changes in magnetic field over time. The first term on the right side of the equation is the convective term. This term describes how the motion of the plasma affects the magnetic field. The second term is the diffusive

term which describes the motion of the magnetic field through the plasma [*Baumjohann and Treumann*, 2012].

$$\frac{\partial \vec{B}}{\partial t} = \nabla \times (V \times \vec{B}) \; + \; \eta \nabla^2 \vec{B} \tag{1.1}$$

The ratio between convection and diffusion is described by the magnetic Reynolds number and equation 1.2 shows how the magnetic Reynolds number is calculated [*Baumjohann and Treumann*, 2012].

$$R_m = \frac{l_0 v_0}{\eta} \tag{1.2}$$

where v_0 is the typical plasma speed, $\eta = \frac{1}{\mu_0 \sigma}$, μ_0 is the permeability of free space, σ is the conductivity of the plasma and l_0 is the characteristic length over which the field varies. When R_m is very small the diffusive term dominates and the magnetic field diffuses through the plasma. When R_m is large the conductivity term dominates, leading to the frozen-in effect.

1.3.2 Particle motion in electromagnetic fields

This subsection provides an overview of the interactions of electric charges with electromagnetic fields, and the mechanisms which drive IMF-plasma coupling and particle precipitation into the ionosphere.

Lorentz force and gyration

Equation 1.3 is the equation of motion for a charged particle within electric and magnetic fields governed by the Lorentz force.

$$\vec{F_L} = m\frac{d\vec{v}}{dt} = q(\vec{E} + \vec{v} \times \vec{B}) \tag{1.3}$$

In this equation the force on the particle is dependent on the charge of the particle and the magnitude of the electric and magnetic fields. Moreover, the force depends on the perpendicular component of the velocity vector. The

electric field applies a force within its plane while the magnetic field applies a force perpendicular to both the particle's motion and the magnetic field. In the case of an absent electric field and homogeneous magnetic field along the direction of the particle's motion, the particle will experience gyration around the magnetic field. To find the periodicity and radius of the gyration, the Lorentz force which is now $\vec{F_L} = q(\vec{v} \times \vec{B})$, is set equal to the centripetal force for circular motion. Taking into account only the velocity perpendicular to the magnetic field, equation 1.4 is obtained:

$$qv_{\perp}\vec{B} = \frac{mv_{\perp}^2}{r_L} \tag{1.4}$$

where r_L is the Larmor radius. The Larmor radius is therefore $r_L = \frac{mv_{\perp}^2}{qv_{\perp}\vec{B}}$ and the gyro period, which is the time taken to complete an "orbit" around the gyro centre, is $T_L = \frac{2\pi r_L}{v_{\perp}}$. The direction of the orbit depends upon the charge of the particle, positive (negative) charges have a clockwise (anticlockwise) motion around the magnetic field/ gyro centre.

Drifts of particles in Electromagnetic fields

Figure 1.2 is a table showing the drifts of positive and negative charges under various fields with a magnetic field in the direction out of the page. Example one is the case for a homogeneous magnetic field, example two is the case for a homogeneous electric field perpendicular to the magnetic field pointing out of the page, and example three is the case including the gravitational force. The gravitational force is negligible compared to electric and magnetic fields.

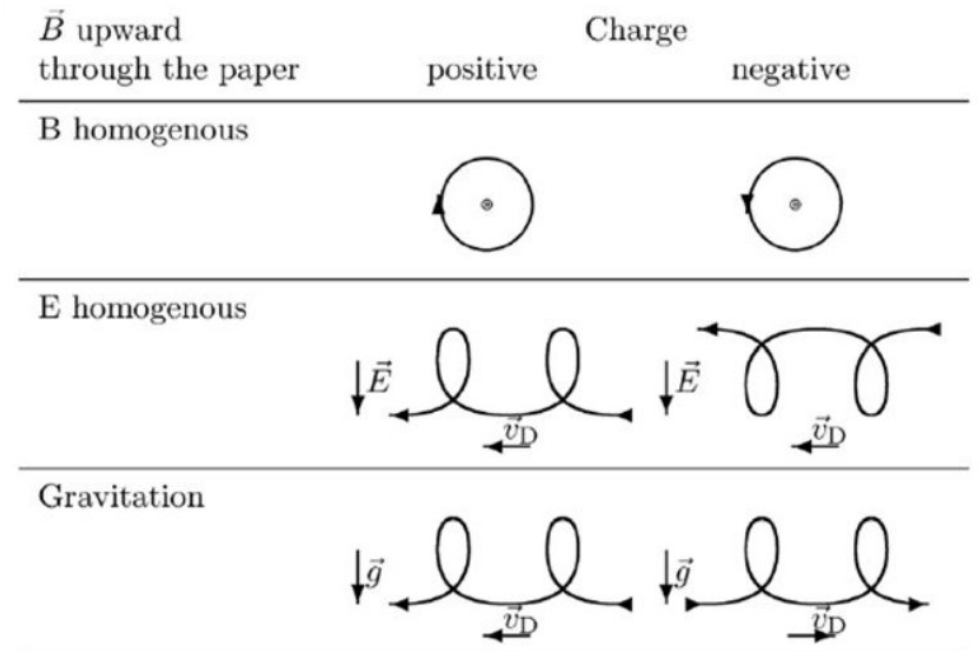

Figure 1.2: Drifts of charged particles in various types of fields. After *Kallenrode* [2013].

The first example was described in the previous subsection, the charges follow circular motion around the magnetic field when looking along the direction of the magnetic field or when there is no velocity in the direction of the magnetic field, with the direction of the particle's motion being dependent on the charge of the particle. The second example is taking into account a homogeneous electric field which results in an overall drift in a direction perpendicular to the magnetic and electric field, this is often referred to as $\vec{E} \times \vec{B}$ drift. The drift direction is independent of charge, however the gyro motion of the particles in the drift is dependent on the charge much in the same way as example one. Example two and three can be generally described using equation 1.5, which shows the drift velocity of a particle within a magnetic field with a force applied perpendicular to the magnetic field.

$$\vec{v_D} = \frac{1}{q} \frac{\vec{F} \times \vec{B}}{\mid \vec{B} \mid^2} \tag{1.5}$$

When changing the force in equation 1.5 to be $\vec{F} = \vec{E}q$, a force due to an electric field, the charge dependence of the drift velocity is lost. When placing the force in equation 1.5 equal to $\vec{F} = m\vec{g}$, a force due to a gravitational field, the charge dependence of the drift velocity remains. For a charged particle undergoing a force from a gravitational field perpendicular to a magnetic field the drift velocity direction is dependent on the charge of particle. The gyro motion remains the same for both examples, clockwise (anti clockwise) for positive (negative) charges. The velocity of the particle in the direction of the electric field has a charge dependence related to the electric force applied whereas the force from the gravitational field is independent of charge and is always applied in the same direction. In example two, the charge dependence of the direction of the force from an electric field is the reason why there are two different gyration paths for the positive and negative charges. The paths appear to be mirrored along the direction of the drift velocity given by $\vec{E} \times \vec{B}$. In example three, the force from the gravitational field, creates two different gyration paths for the positive and negative charges. The paths appear to be mirrored along direction of the gravitational field.

1.4 The Earth's magnetosphere

The geomagnetic field is an important barrier between interplanetary space and the Earth's atmosphere. The presence of a magnetic field around the Earth reduces the effects of the solar wind and IMF on the Earth's environment. Without the effects of the solar wind the geomagnetic field could be approximated to a tilted dipole magnetic field and would extend uniformly out into interplanetary space. Figure 1.3 depicts the interaction of the solar wind and the IMF with the near-Earth environment and shows how the shape and structure of the Earth's magnetosphere is dominated by solar influences.

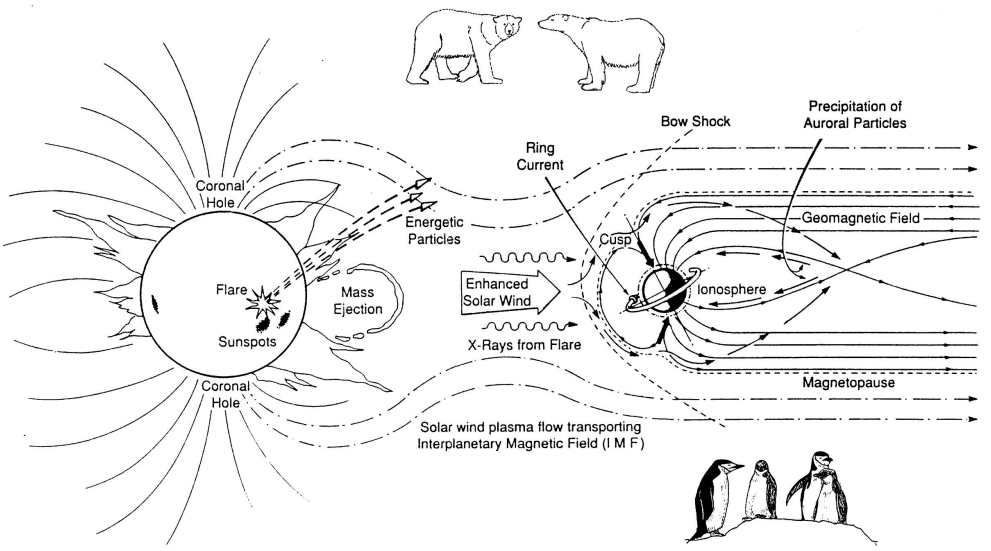

Figure 1.3: Representation of the interaction of the Sun on the Earth's environment in terms of the interplanetary magnetic field and solar wind. After *Hunsucker and Hargreaves* [2007].

There are a number of features of the magnetosphere that can be identified. Describing them from the solar wind perspective, the first feature is the bow shock, where the solar wind is slowed until it becomes subsonic. The solar wind continues until it reaches the magnetopause, where there is a pressure balance between the solar and geomagnetic fields. When the geomagnetic field is compressed the magnetopause current increases, which strengthens the Earth's magnetic field and restores a balance between the fields. Finally one encounters the magnetotail which is often described as open magnetic field lines being dragged downstream of the Sun and into interplanetary space.

1.4.1 Magnetic reconnection

Magnetic reconnection is a process that occurs when magnetic field lines of opposite polarity interact under pressure. Magnetic reconnection is an important mechanism for a number of solar processes. For the scope of this thesis one of the relevant processes is the reconnection of the IMF with the

geomagnetic field, which results in the IMF being coupled with the Earth's magnetic field lines. This process occurs at the magnetopause, more likely when the IMF is orientated southward (B_z is negative). At the magnetopause an inflow of magnetic flux in the B_x direction results in a perpendicular outflow of magnetic flux parallel to the two geomagnetic poles. This process is depicted in Figure 1.4.

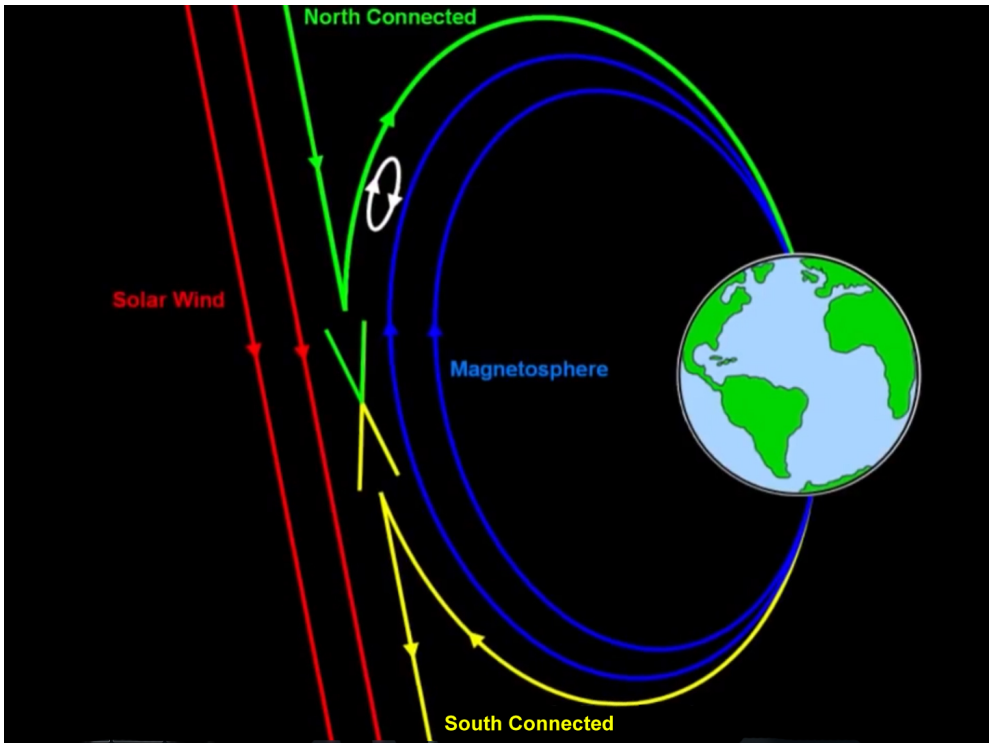

Figure 1.4: Sketch depicting the magnetic reconnection at the magnetopause where X marks the point of reconnection. Adapted from [*Zell*, 2015].

In the reconnection process described, the magnetic field lines will convect over the poles and then reconnect in the tail, after which the IMF continues into interplanetary space. There can be some rarer occurrences of magnetic reconnection under northward IMF conditions. In this case the IMF reconnects with an open magnetic field in the magnetotail and the field lines not connected to the poles are carried out by the solar wind into interplanetary

space [*Russell*, 1972; *Dungey*, 1961].

1.5 The Earth's ionosphere

The ionosphere is one of the Earth's upper atmospheric layers, located at approximately 50–1000 km altitude, and is characterised by the presence of ions and electrons in addition to neutral particles. Various phenomena can be a source of ions within the ionosphere. These include photoionisation due to solar radiation and particle precipitation.

1.5.1 Ionospheric layers

The ionosphere has defined layers at different altitudes that exhibit distinctly different electron densities and density gradients. Figure 1.5 depicts the electron density profile for a general dayside ionosphere. For the dayside there are normally three ionospheric layers: D, E, F.

D-layer

The D-layer lies between 50–90 km in altitude. Between 50–70 km the main source of ionisation is cosmic rays [*Tolmacheva*, 1970; *Velinov et al.*, 2009]. The solar sources of ionisation that contribute to the D-layer formation is mainly hard X-rays. The dominant neutral molecules in the D-layer are N_2 and O molecules, which can be seen in Figure 1.6, while the ionised component of the D-layer is comprised primarily of O_2^+ and NO^+ [*Tolmacheva*, 1970; *Pfaff*, 2012]. At night, the D-layer weakens due to reduced electron/ion production.

E-layer

The E-layer lies between approximately 90–140 km in altitude and the peak density of the E-layer is situated at around 110 km. The main source of ionisation for the E-layer is soft solar X-rays. Figure 1.6 shows the dominant neutral molecules for the E-layer which are N_2 and O. N_2 is the most dominant neutral species whereas NO^+ ions are the dominant ion species [*Pfaff*, 2012]. The E-layer is strongest during the day and weakens at night.

F-layer

The F-layer is the ionospheric layer between approximately 140–1000 km. The F-layer can sometimes be split into two layers, F1 and F2. The F1-layer lies between approximately 140–210 km and the main source of ionisation is from solar extreme ultraviolet rays. It has a peak electron density at around 190 km in altitude. As shown in Figure 1.6, the composition of the F1-layer for neutrals is dominated by N_2 and O molecules [*Pfaff*, 2012]. The F2-layer extends from 210 km up to 1000 km. The layer has a peak in electron density at approximately 350 km in altitude. The F2-layer is comprised primarily of O molecules and $O+$ ions. At higher altitudes the neutral atmosphere is referred to as the thermosphere and at this region the neutral composition is dominated by hydrogen and helium [*Pfaff*, 2012]. The E-and F-layer are always present however, during periods with a weak ionosphere the defined shape of the E-and F-layers seen in figure 1.5 is less prominent. A weak ionosphere such as the night time ionosphere can see the loss of the clear variation of the F1-and F2-layer leading to the two layers being defined as one F-layer. Other examples of a weakened ionosphere can be related to the solar cycle. Solar irradiance follows the solar cycle much in the same way as other solar parameters such as the number of sunspots, position of sunspots, solar magnetic activity and solar wind speed. The variation of solar irradiance leads to a significant and measurable difference in electron density profiles in the ionosphere during solar minimum and solar maximum [*Liu et al.*, 2011; *Kelley*, 2009].

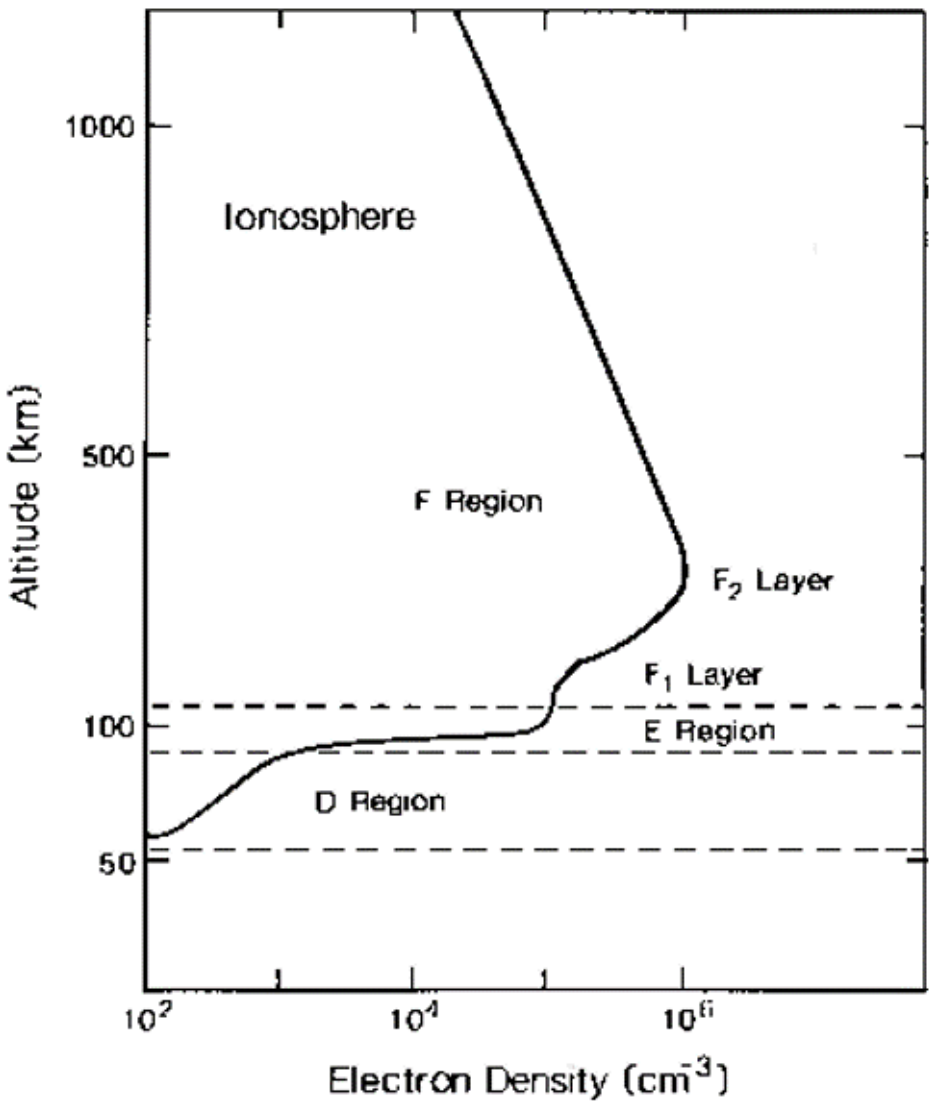

Figure 1.5: Electron density profile of the ionosphere. From [*Kivelson*, 1995]

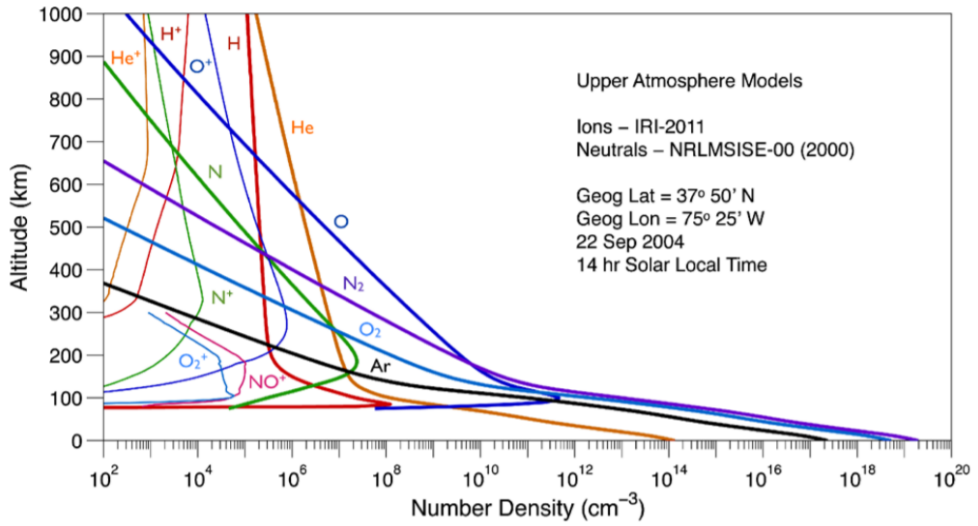

Figure 1.6: Ionospheric composition with altitude. From *Pfaff* [2012]

1.5.2 Ionospheric irregularities

Electromagnetic forces can produce periodic electron density structures called ionospheric irregularities [*Cole*, 1963]. To show the requirements for the formation of irregularities the continuity equation for charged particles is introduced and this can be written as:

$$\frac{\partial n_e}{\partial t} = q - L - \nabla \cdot (n_e \vec{v}_D) \tag{1.6}$$

In this equation q is the rate of production of electrons, L is the loss rate for the electrons and $\vec{v}_D$ is the drift velocity for the electrons. Setting $nv_D^{\rightarrow} = \phi \vec{j} \times \vec{B}$, where $\vec{j}$ is the current density relative to the drift velocity of the electrons, $\vec{B}$ is the total geomagnetic field, and ϕ is a scalar containing the mass of ions and electrons and the collision frequencies of ions and electrons, the transport term in equation 1.6, can be set equal to [*Cole*, 1963]:

$$\nabla \cdot (n_e \vec{v}) = \vec{j} \times \vec{B} \cdot \nabla \phi + \phi \vec{B} \cdot \nabla \times \vec{j} - \phi \vec{j} \cdot \nabla \times \vec{B} \tag{1.7}$$

*L*YR backscatter properties

Therefore the continuity equation becomes:

$$\frac{\partial n_e}{\partial t} = q - L - \vec{j} \times \vec{B} \cdot \nabla\phi - \phi\vec{B} \cdot \nabla \times \vec{j} + \phi\vec{j} \cdot \nabla \times \vec{B} \tag{1.8}$$

One can see from equation 1.8 that in order to have a production of electron density irregularities it is necessary to have a gradient of ϕ in the opposite direction to $\vec{j} \times \vec{B}$ or a component of $\nabla \times \vec{j}$ in the opposite direction to the geomagnetic field. The last term of the equation gains importance only in the case of strong auroral electrojets, therefore most of the time it can be neglected. Strong large-scale irregularities occur when the variation of the electron density is approximately equal to the electron density itself. The typical spatial scale size for these instabilities is approximately 1000 km. Weak small-scale irregularities or decameter irregularities occur when the variation of the electron density is significantly smaller compared to the electron density itself. With SuperDARN it is possible to detect decameter electron density irregularities since the wavelength of the transmitted signal is approximately 30 m. Two processes which are favorable to the formation of ionospheric irregularities at high latitudes are particle precipitation regions and generation of polar cap patches.

1.5.3 High latitude particle precipitation

The two most frequent particle precipitation processes occurring in the high latitude northern ionosphere are described in this section.

Cusp precipitation

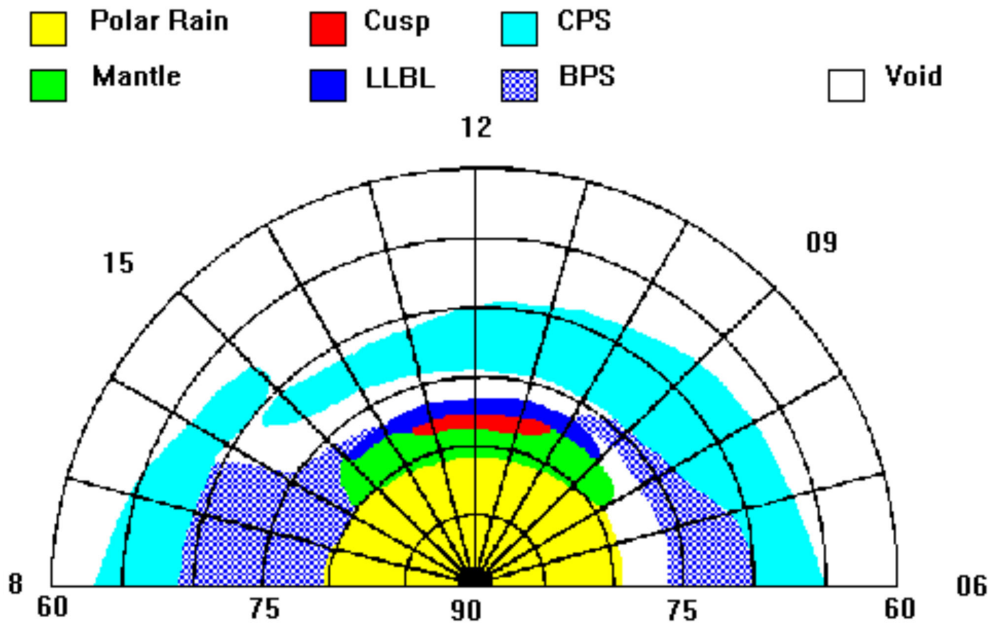

Figure 1.7: Precipitation regions. Adapted from *Newell and Meng* [1992]

The cusp is a region of the Earth's magnetosphere and ionosphere and it is shown in Figure 1.3 and 1.7. The cusp is encased by open magnetic field lines that stretch out to the magnetotail and by the closed magnetic field lines on the dayside of the geomagnetic field [*Russell*, 2000; *Shi et al.*, 2012; *Johnsen*, 2013]. The cusp was predicted first by Chapman and Ferraro when they were describing a model for the magnetosphere and later discovered in 1971. By studying the energies of the cusp particles it was found that they have a solar wind origin [*Heikkila and Winningham*, 1971]. When discussing cusp precipitation one must first consider the processes involved in particle entry into the cusp region. Entry from the ionosphere, such as through ionospheric flows, is assumed to be minimal in comparison to other entry mechanisms [*Sandahl*, 2003]. The solar wind particles can enter the cusp in several ways: they can enter due to dayside reconnection from lower latitudes, from reconnection at the tail lobes, from reconnection with high latitude open

field lines or from direct entry into the cusp [*Sandahl*, 2003].

The occurrence of precipitation within the cusp region depends on the energy of the particles entering the cusp. Particles entering due to reconnection have greater energies and are much more likely to precipitate. The position of the cusp can vary depending on the IMF conditions and the location of reconnection between the IMF and the geomagnetic field. Due to the shape of the geomagnetic field, given by the tilt of the magnetic field axis, the cusp can be detected in both hemispheres. The axis tilt gives asymmetry to the latitudinal positions of the cusps in the two hemispheres [*Shi et al.*, 2012; *Russell*, 2000].

During geomagnetic quiet periods the cusp can reach as high as 84° in geomagnetic latitude while in extreme geomagnetic active periods it can reach as low as 61° geomagnetic latitude. On average, the position of the cusp is considered to be around 78° geomagnetic latitude with approximately 5° in width [*Hunsucker and Hargreaves*, 2007; *Pitout et al.*, 2006; *Wing et al.*, 2005]. This makes Svalbard an ideal location for ground-based observations of the cusp. The IMF conditions drive the geomagnetic conditions and variations in the By and Bz components of the IMF have implications on the shape, size, position and plasma properties of the cusp. Many studies, such as the ones by *Sandahl* [2003] and *Pitout et al.* [2006], have found that the geomagnetic latitude of the cusp is controlled by the Bz component. Whereas, the By component and the direction of the solar wind eastward or westward has a significant effect on the position of the cusp in terms of magnetic local time [*Sandahl*, 2003; *Pitout et al.*, 2006; *Wing et al.*, 2005]. When discussing the northward/southward orientation of the IMF, studies have shown that a northward IMF can shift the position of the cusp to earlier MLTs [*Sandahl*, 2003].

To find the SuperDARN radar signatures of the cusp, initial studies correlated satellite data, where cusp signatures are known, with variations in parameters measured by the radar. *Baker et al.* [1995] pursued this study using the combination of DMSP (Defense Meteorological Satellite Program) satellites and the PACE (Polar Anglo-American Conjugate Experiment) radars and found that enhanced spectral widths with average values of around $200\,\mathrm{m\,s^{-1}}$, with

a range between 120–320 m s^{-1}, were associated with cusp detection. *Chisham and Freeman* [2003] showed that SuperDARN radars observe a sharp transition from low to high spectral width at the low latitude boundary of the cusp. This feature has been used in multiple studies to determine the location of the cusp boundaries [e.g. *Chisham and Freeman*, 2004; *Chen et al.*, 2016].

Substorm-induced precipitation

Magnetic reconnection in the geomagnetic tail has been discussed in section 1.4.1. This process is the driving force of the high energy features observed on the night side. Reconnection can occur in the tail regularly, however substorms are more infrequent and occur when large amounts of stored magnetic energy is released from the tail and transferred to the local plasma. This accelerates the plasma towards the poles leading to particle precipitation and auroral displays.

Substorms can be described through three phrases: the growth phase, the expansion phase and the recovery phase. *Akasofu* [1964] initially described substorms as having two phases, the expansion phase and the recovery phase. However, later work by *McPherron* [1970] identified an earlier phase, the growth phase. The growth phase is characterised by a loading of the energy in the magnetotail and can be identified by a deviation from the quiet time measurements of the horizontal component of the geomagnetic field (H-component) in the auroral zone [*McPherron*, 1970]. The expansion phase can last for 10 to 30 minutes and involves the process of releasing the stored magnetic energy producing a poleward acceleration of the tail plasma along the field lines. The expansion phase is often identified by a negative bay within the H-component of the magnetic field. This is associated with an expansion of the westward electrojet. A number of studies have discussed the positive bays often visible in magnetometers, at lower latitudes than the negative bays, with similar times [*Ahn et al.*, 2005; *Lyons et al.*, 2013]. However, due to the high latitude scope of this thesis it will not be visible in the magnetometer data used. The recovery phase is the process of magnetospheric relaxation, characterised by the reduced energy in the auroral displays and the slow return of magnetometer data to quiet time conditions. This process

can take from 1-2 hours or even longer depending on the substorm. Due to the longevity of this phase it can be common for it to be interrupted by the onset of another substorm, leading to the features of this phase to be obscured [*Partamies et al.*, 2011; *Forsyth et al.*, 2015; *Nagai et al.*, 1983; *Ahn et al.*, 2005; *Lyons et al.*, 2013; *Johnsen*, 2013].

1.5.4 Ionospheric electron densities

The ionosphere is often probed using radio waves. To understand the propagation path of radio waves the ionosphere is modeled with a series of uniform, horizontal slabs with a thickness of a few wavelengths [*Hargreaves*, 1992], see Figure 1.8 for the detailed illustration.

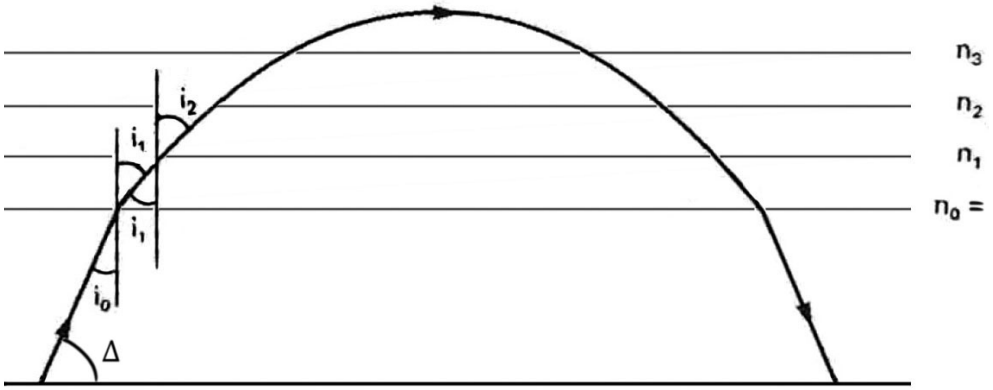

Figure 1.8: Propagation of a radio wave through uniform, horizontal ionospheric slabs.

The path of the transmitted signal of the radar is bent as it propagates through the ionosphere and this is due to a decreasing refractive index and an increasing plasma frequency. Therefore, the rays at greater altitudes are refracted less than the ones at lower altitudes. In this thesis the electron densities are calculated using Snell's law and an approximated form of the Appleton-Hartree equation. This has been implemented by *Gillies et al.* [2009] for SuperDARN radars.

The Appleton-Hartree equation is approximated assuming that the absorption

of the transmitted radar signal by the ionosphere is small, there are no effects from the geomagnetic field and the plasma is collisionless. According to Snell's law, for each refractive index boundary it is possible to obtain:

$$\begin{aligned} n_0 \sin i_0 &= n_1 \sin n_1 \\ n_1 \sin i_1 &= n_2 \sin n_2 \\ n_2 \sin i_2 &= n_3 \sin n_3 \\ &\vdots \\ n_{r-1} \sin i_{r-1} &= n_r \sin n_r \end{aligned}$$

where n_0, n_1,...n_r are the refractive indices for each boundary layer and i_0, i_1,...i_r are the angles of incidence to the medium for each slab. It follows that $n_0 \sin i_0 = n_r \sin n_r$. At the reflection point $i_r = 90°$ and the refractive index of neutral air n_0 can be set equal to 1. Therefore, it is possible to assume:

$$\sin i_0 = n_r \Rightarrow \sin i_0 = n \tag{1.9}$$

The approximated form of the Appleton-Hartree equation used is:

$$n^2 = 1 - \frac{\omega_P^2}{\omega_R^2} \tag{1.10}$$

where ω_P^2 is the plasma frequency (natural oscillation frequency of the plasma) and ω_R^2 is the frequency of the radar. From equation 1.10 and equation 1.9 it is possible to derive the following equation for the plasma frequency:

$$\frac{\omega_P^2}{\omega_R^2} = 1 - n^2 = 1 - \sin i_0^2 = \cos i_0^2 \Rightarrow \omega_P = \omega_R \cos i_0 \tag{1.11}$$

The plasma frequency is also proportional to the electron density N at the reflection height, the electron charge e, the electron mass m_e and the permittivity of free space ϵ_0 with the following relation:

*L*YR backscatter properties

$$\omega_P = \left(\frac{Ne^2}{4\pi^2 \epsilon_0 m_e} \right)^{\frac{1}{2}} \tag{1.12}$$

The plasma frequency is expressed in Hertz. Substituting 1.11 into 1.12 the equation for the electron density at the reflection height becomes:

$$N = \frac{\omega_R^2 \cos i_0^2 4\pi^2 \epsilon_0 m_e}{e^2} \tag{1.13}$$

where $i_0 = 90° - \Delta$ and Δ is the elevation angle or angle of arrival.

1.5.5 Radio-wave propagation in the ionosphere

The hypothesis of a reflecting layer in the upper atmosphere was first introduced by G. Marconi when he found out that waves of certain lengths could cover great distances during his transatlantic experiment in 1901. The existence of an ionosphere was finally established by E. V. Appleton in 1924 [*Beynon*, 1975].

In order to have ionospheric reflection from geomagnetic field aligned electron density irregularities, the HF radio waves transmitted by the radar need to be orthogonal to the target [*Bates and Albee*, 1970]. SuperDARN radars exploit the refractive property of the ionosphere to meet this condition at high latitudes.

The real propagation path of the transmitted signal is unknown [*Villain et al.*, 1984]. However, it is possible to describe HF radio propagation with virtual ray paths assuming that they travel in straight lines as they would behave *in vacuo*. There are many propagation modes and Figure 1.9 shows some of them.

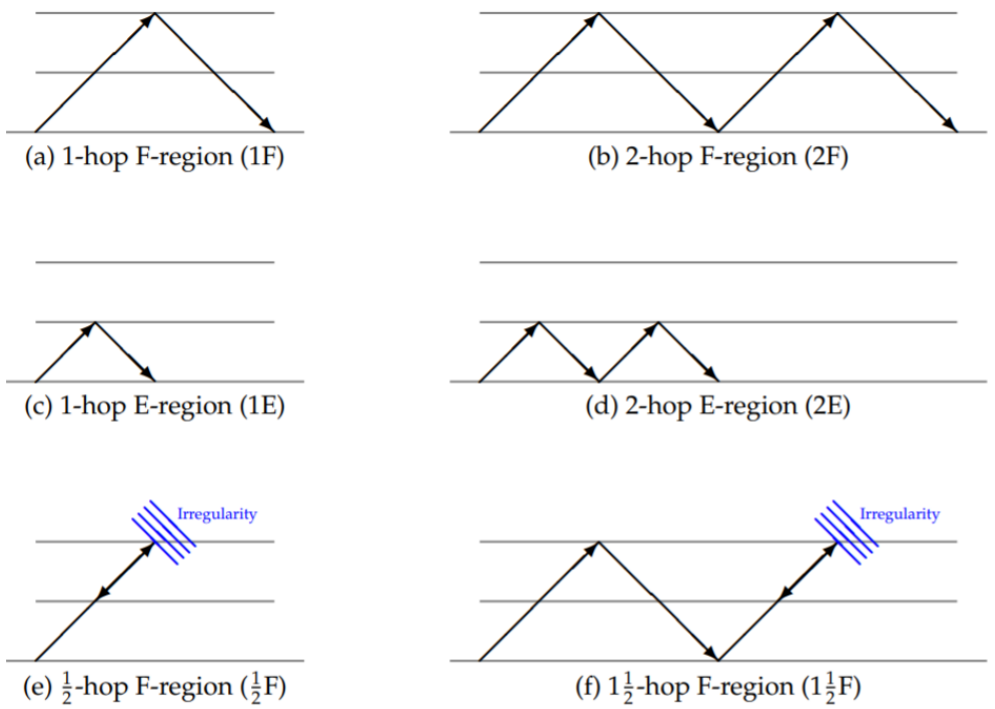

Figure 1.9: Virtual ray paths for various ionospheric propagation modes. From *Bland* [2012].

A hop length is the hypothetical ground distance covered by a radio signal which has traveled between two ground-based locations with a single ionospheric reflection. Multiples of 1-hop propagation mode only increase the distance between the number of hypothetical ground-based locations. Odd-integer numbers of half-hops are representing virtual ray paths for which the received signal has been scattered in the ionosphere rather than on the ground (Figure 1.9 e and f).

Almost all the backscatter detected by the Longyearbyen radar is $\frac{1}{2}$-hop scatter due to the weak polar ionosphere.

The SuperDARN radars receive backscatter from three types of scattering targets. The backscatter from decameter-scale electron density irregularities aligned with the Earth's magnetic field is called ionospheric backscatter and

it is the major type of backscatter studied by the SuperDARN community. Ground scatter is caused by oceans and lands whereas meteor scatter arises from meteor plasma trails in the ionosphere.

Chapter 2

Instrumentation

Presented in this chapter is a description of the Longyearbyen SuperDARN radar and the multipulse sequence method used to determine the backscattered power, line-of-sight Doppler velocity and Doppler spectral width. The line-of-sight Doppler velocity and the Doppler spectral width measurements are used in this thesis to study the features of the ionospheric structure and dynamics which are observed with the LYR radar.

Moreover, the calculation to determine the angle-of-arrival of the received backscatter is presented. The elevation angle measurements are used to estimate the reflection altitude of the backscatter, and to estimate the ionospheric electron density.

2.1 SuperDARN

The Super Dual Auroral Radar Network (SuperDARN) [*Greenwald et al.*, 1985, 1995] is a network of more than 30 HF coherent-scatter radars with similar characteristics operating in the Northern and Southern hemispheres. The radars operate continuously and their fields-of-view cover a large area from mid-latitudes to the polar regions. SuperDARN is used to study dynamic processes in the Earth's magnetosphere-ionosphere system and the structure of the Earth's ionosphere. It contributes to the study of global iono-

spheric plasma convection, field aligned currents, magnetic reconnection, MHD waves, high latitude plasma structures and a range of other magnetospheric and ionospheric phenomena [*Chisham et al.*, 2007].

2.1.1 The SuperDARN array

The SuperDARN radar of interest for this thesis is located in Longyearbyen on the Svalbard Archipelago (geographic coordinates: 78.153°, 16.074°). This radar began official operations in October 2016. Figure 2.1 shows the radar field-of-view, where latitudes and longitudes are in magnetic coordinates.

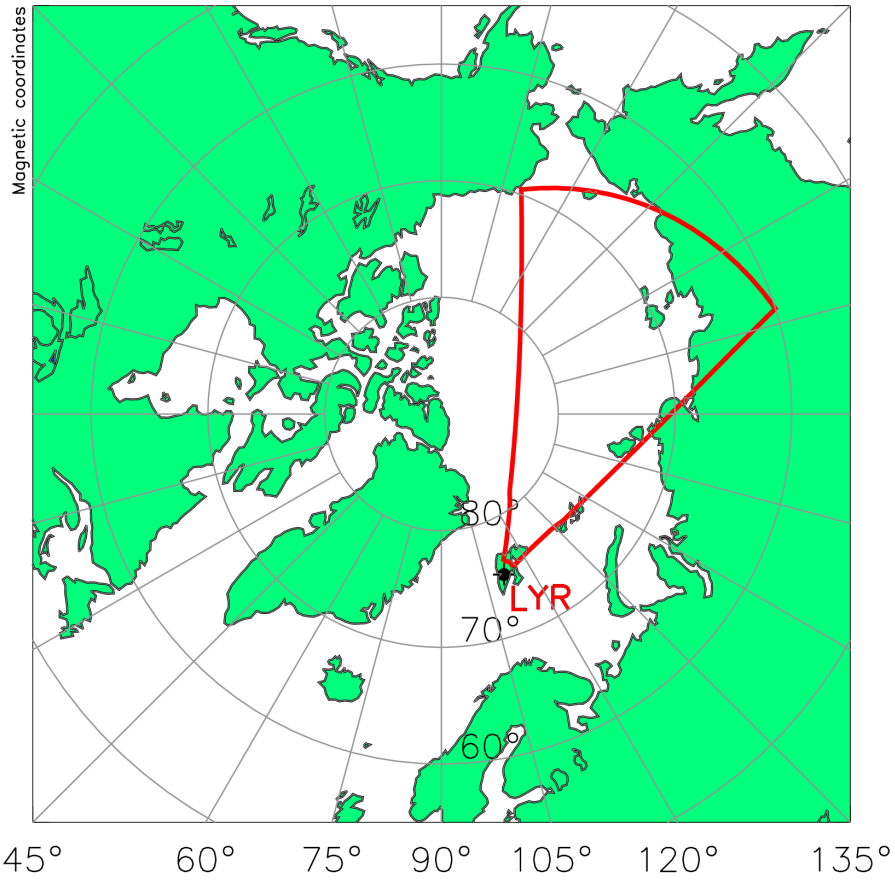

Figure 2.1: Longyearbyen radar field-of-view

The radar consists of a linear array of 16 twin-terminated folded dipole antennas transmitting and receiving in the frequency range 8–20 MHz. Constructive interference between each antenna radiation pattern allows the formation of a narrow beam which can be electronically steered in 16 different azimuthal directions within a 52° sector. The directions of the interference maxima depend on the time delay (phase shift) in the transmitted signals between adjacent antennas. The 16-beam scan creates a field-of-view that extends from 180 km to 3555 km in range and in total there are 75 range gates, each with 45 km resolution. Each radar beam sends sequences of short pulses for approximately 3 s such that a complete scan of the radar field-of-view takes 1 minute.

2.1.2 The SuperDARN multipulse sequence method

SuperDARN radars operate using a multipulse sequence method to measure the backscattered power (signal-to-noise ratio), line-of-sight Doppler velocity and Doppler spectral width. The pulse sequence used typically consists of 7 or 8 pulses. For simplicity, the basic features of the multipulse method are illustrated here for a 2-pulse sequence. Figure 2.2 is a graphic representation of two pulses sent at times t_0 and $t_0 + \tau$ and the transmitted signals are reflected at three ranges, d_-,d_0 and d_+.

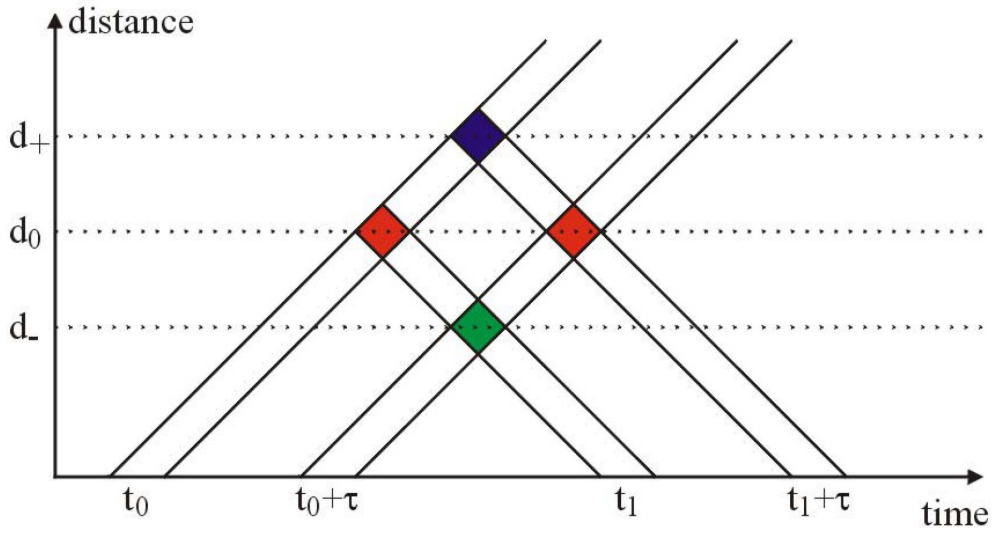

Figure 2.2: Illustration of a 2-pulse sequence. Adapted from *McWilliams et al.* [2003]

Two pulses are sent separated by a time τ. The first pulse is reflected at range d_0 and returns to the radar at time t_1. At time t_1 the signal from range d_- is also received. At time $t_1 + \tau$ the transmitted signal is reflected from ranges d_+ and d_0. The amplitude measured at t_1 is $A(t_1) = A_1(d_0) + A_2(d_-)$ and the amplitude measured at t_2 is $A(t_1 + \tau) = A_1(d_+) + A_2(d_0)$. The autocorrelation function (ACF) for the 2-pulse sequence is [*Baker et al.*, 1988]:

$$A(t_1) \cdot A(t_1 + \tau) = (A_1(d_0) + A_2(d_-)) \cdot (A_1(d_+) + A_2(d_0)) \tag{2.1}$$

where A_1 and A_2 are the amplitudes of the received signals at times t_1 and $t_1 + \tau$. To reduce the effect of the uncorrelated signals from ranges d_- and d_+, ACFs from up to 30 multipulse sequences are averaged together over the 3 s integration time. One then obtains:

$$\begin{aligned} \langle A(t_1) \cdot A(t_1 + \tau) \rangle = \langle A_1(d_0) \cdot A_2(d_0) \rangle + \langle A_1(d_0) \cdot A_1(d_+) \rangle \\ + \langle A_2(d_-) \cdot A_1(d_+) \rangle + \langle A_2(d_-) \cdot A_2(d_0) \rangle \end{aligned} \tag{2.2}$$

where the first term on the right side of the equation is the one relevant for

the backscatter from range d_0. As a last step one can approximate:

$$\langle A(t_1) \cdot A(t_1 + \tau) \rangle \sim \langle A_1(d_0) \cdot A_2(d_0) \rangle \sim A e^{i\omega\tau} \tag{2.3}$$

The exponential term contains the phase information which is used for estimating the mean line-of-sight Doppler velocity in the scattering volume and Doppler spectral width. The parameters are calculated using the FITACF computer program developed especially for SuperDARN radars [*SuperDARN Data Analysis Working Group*, 2018]. An important remark is that the ACF amplitude decreases when increasing lag time due to decorrelation of the ionospheric plasma.

2.1.3 Doppler frequency shift

As previously mentioned the information regarding the mean line-of-sight Doppler velocity is contained in the phase. In particular, it is possible to calculate the velocity once the phase shift is obtained. The relation for two pulses separated by a time τ is:

$$v = \frac{c}{4\pi\tau f_0}\Delta\phi \tag{2.4}$$

where f_0 is the transmitted frequency of the radar and $\Delta\phi$ is the phase shift between two pulses. The velocity v is the line-of-sight velocity. By convention, positive velocities represent motion of plasma towards the radar and negative velocities represent motion of plasma away from the radar.

2.1.4 Elevation angle (angle-of-arrival) calculation

Most SuperDARN radars, including the Longyearbyen radar, have a secondary antenna array situated 100 m away from the main array. This array is receive-only and the phase difference between the two arrays is used to determine the elevation angles [*Milan et al.*, 1997]. Figure 2.3 shows the radar site consisting of the two arrays. The secondary array can also be referred to as the interferometer array.

*L*YR backscatter properties

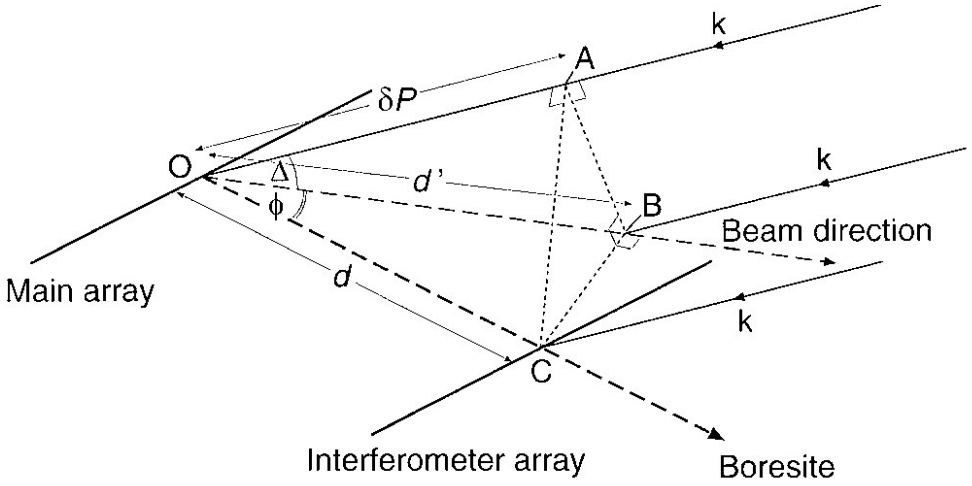

Figure 2.3: Geometry of the two SuperDARN arrays with the interferometer array being in front of the main array. From *Milan et al.* [1997]

The segment OA is denoted as δP and it is the path difference between the backscatter received at the main array and the interferometer array. One can set δP equal to $\delta P = \frac{\Psi}{|\vec{k}|} = \frac{\Psi\lambda}{2\pi}$, where $|\tilde{k}|$ is the wave vector and Ψ is the phase difference between the two signals received at the two arrays. The elevation angle Δ is the angle related to the inclination of the segment OA and is given the following relation:

$$\cos\Delta = \frac{\delta P}{d'} = \frac{\Psi}{|\vec{k}|\, d\cos\phi}, \tag{2.5}$$

where $d' = d\cos\phi$, with ϕ being equal to the azimuthal angle formed by $\angle$BOC and d is the distance between the main array and the interferometer. Introducing the new variable ϕ_0 for the azimuthal angle when $\Delta = 0°$ and substituting the relation $\cos^2\Delta\cos^2\phi + \sin^2\Delta = \cos^2\phi_0$ into equation 2.5 as shown by *Milan et al.* [1997] one obtains:

$$\sin\Delta = \left(\cos^2\phi_0 - \frac{\Psi^2}{|\vec{k}|^2 d^2}\right)^{\frac{1}{2}} \tag{2.6}$$

It is important to notice that typically the Longyearbyen radar is transmitting at frequencies close to 10 MHz which is equivalent to a wavelength of approximately 30 m. This is smaller than the distance between the main array and the interferometer. This gives rise to an aliasing effect in the phase measurements since the total phase difference Ψ is greater than 2π. The total phase difference between the two received signals is therefore [*Milan et al.*, 1997]:

$$\Psi = \Psi_0 + 2\pi n, \qquad \text{with n=0,1,2...,} \tag{2.7}$$

where n is the number of phase differences within the path traveled by the two signals and $-\pi \leq \Psi_0 < \pi$. In the case of interferometer arrays which are 100 m away from the main array, the maximum elevation angle after which 10 MHz signals are aliased is approximately 45°.

2.1.5 Virtual height

As stated in section 1.5.5, the real path of the transmitted radio wave through the ionosphere is not known. Therefore, to estimate the reflection altitude of the backscatter, an approximation is made assuming that rays travel in straight lines as they would behave *in vacuo* without an ionosphere acting as a refractive medium. This is called the virtual height. Virtual heights in this thesis are calculated according to:

$$h_v = (r^2 + R_E^2 + 2rR_E sin\Delta)^{\frac{1}{2}} - R_E, \tag{2.8}$$

where R_E is the average radius of the Earth (R_E = 6371 km), r represents the different slant-ranges at which the radio wave is reflected back to the radar and Δ is the elevation or angle of arrival measured by the radar.

2.2 Other instruments

The data of the Interplanetary Magnetic Field (IMF) is from the DSCOVR (Deep Space Climate Observatory) satellite. The satellite is orbiting the L1

Lagrangian point and it is run by the National Oceanic and Atmospheric Administration (NOAA) scientific community.

The magnetometer data presented in this thesis are registered by the Longyearbyen magnetometer. The magnetometer is situated in Longyearbyen and is run by the University of Tromsø.

The All Sky Camera keogram is generated using the Sony a7s camera located at the Kjell Henriksen Observatory (KHO) and is owned by the University Centre in Svalbard (UNIS). The Kjell Henriksen Observatory is an optical observatory located in Longyearbyen. At the observatory there are more than 25 optical and non-optical instruments run by different universities and they are employed for research on the middle- and upper atmosphere.

Svalbard EISCAT radar is part of an international scientific association with members from different countries. The EISCAT radars operate in Finland, Norway and Sweden, and they are located above the Arctic circle. The Svalbard radar has two antennas; a 32 meter mechanically-steerable parabolic dish antenna and a 42 meter field-aligned dish antenna. For this thesis the 42 meter dish is used.

Chapter 3

Statistical analysis of electron density irregularities in the northern polar ionosphere

Presented in this chapter is a statistical analysis of the ionospheric backscatter detected with the Longyearbyen SuperDARN radar. This provides information on the electron density irregularities situated in the ionosphere.

3.1 Method

The HF radar used for this study is located in Longyearbyen, on the Svalbard Archipelago, within the polar region of the northern hemisphere. Data collected during year 2017 are used.

The frequency band used for the data analysis runs between 9.8 MHz–9.9 MHz (Channel A) both during the day and during the night. Most of the time Channel A is running the common mode, in which the field-of-view is scanned every 1 minute.

As a first step, potentially unphysical data were removed from the dataset. This included backscatter with very low power (signal-to-noise ratio) or with

spectral widths greater than 400 m s^{-1}. Also, backscatter from ranges greater than 2000 km were excluded. The reason for this is that the ionosphere over Svalbard is too weak to routinely support the 1-hop and 1-$\frac{1}{2}$-hop propagation modes, so echoes detected at ranges greater than or equal to 2000 km are most likely due to noise or radio interference [*Chisham et al.*, 2008]. In the next step, the virtual heights were calculated from the elevation angle measurements according to equation 2.8. The backscatter echo occurrence was calculated in bins of 0.5 hours magnetic local time (MLT) and 10 km of virtual height in order to investigate the virtual heights of the backscatter. The backscatter echos were also organised into 2-dimensional bins of size 0.5 hours MLT and 0.5° magnetic latitude (MLAT).

3.2 Ionospheric layers source of backscatter

Figure 3.1 shows the monthly echo occurrence as a function of MLT and virtual height. The backscatter clearly separates into two populations in virtual height, which correspond to the E- and F-layer of the ionosphere. The F layer is assumed to be above 140 km and the E-layer below this value according to *Bland et al.* [2014].

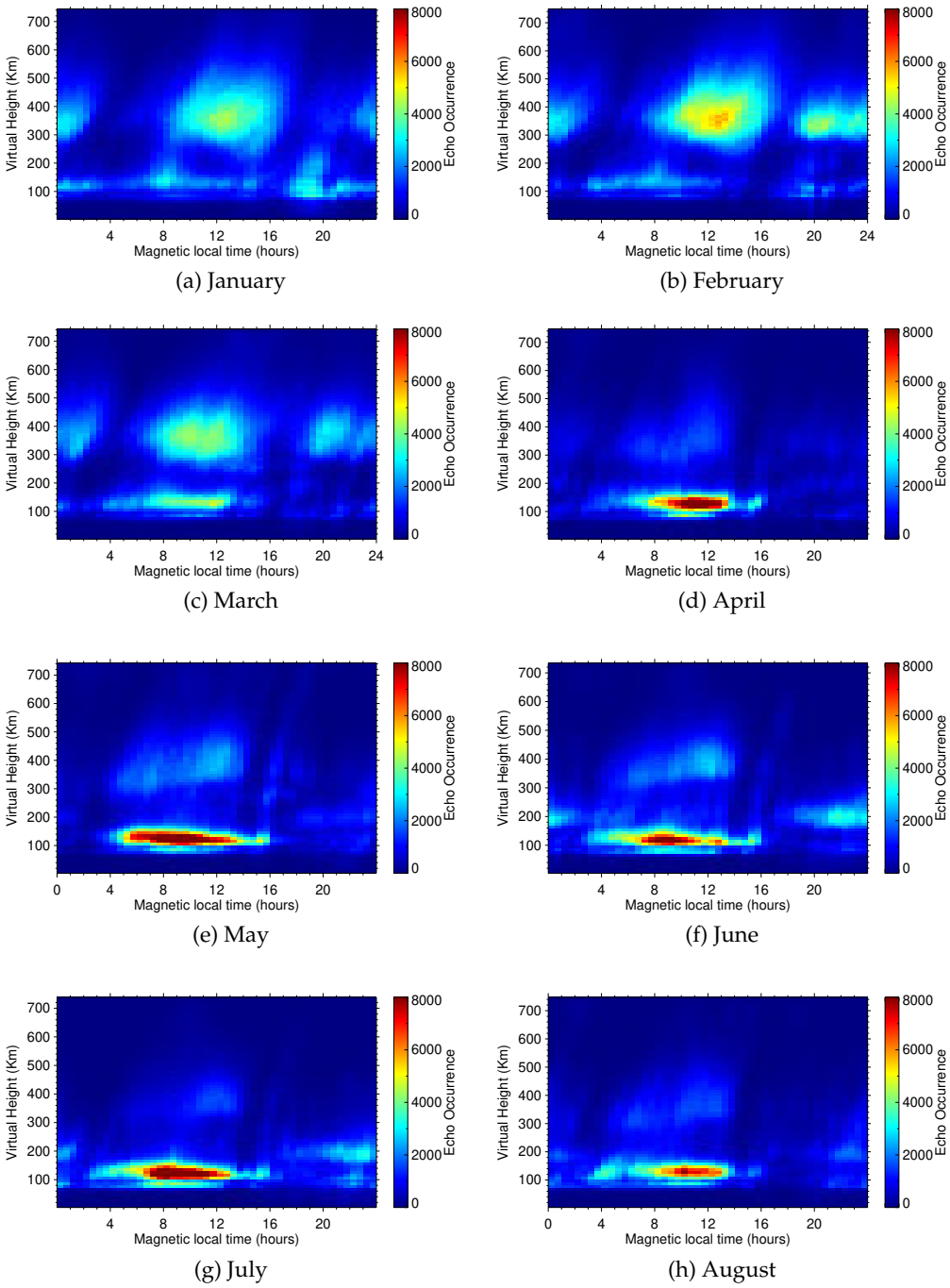

Figure 3.1: Monthly backscatter occurrence statistics for the Longyearbyen SuperDARN radar organized by MLT and virtual height.

*L*YR backscatter properties

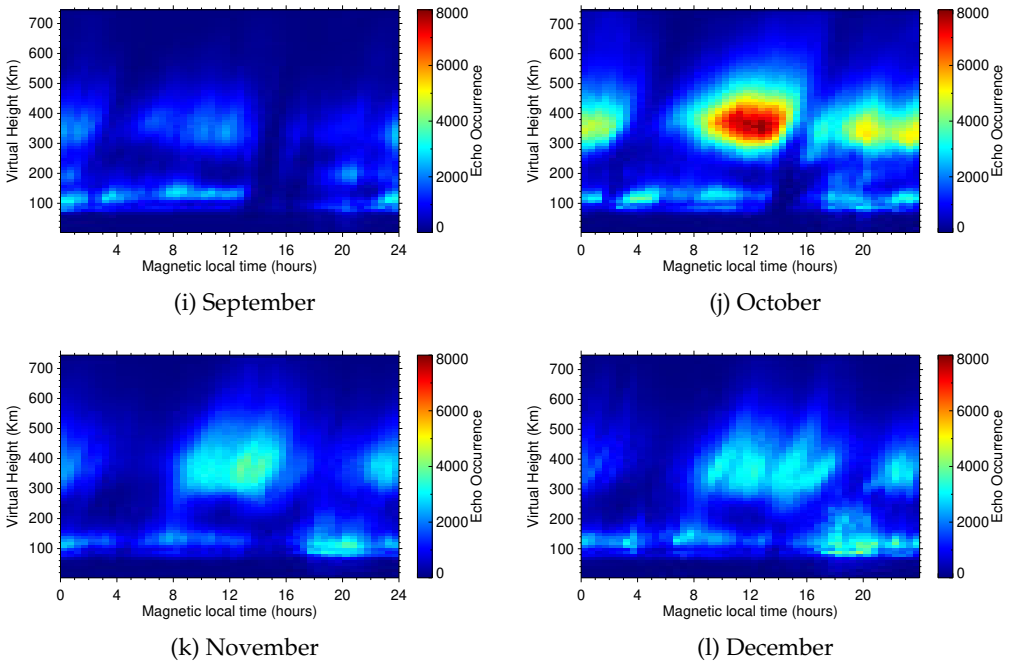

Figure 3.1: Monthly backscatter occurrence statistics for the Longyearbyen SuperDARN radar organized by MLT and virtual height.

3.3 Seasonal variations

There is a seasonal variation in the echo occurrence in the daytime (08–16 MLT for the F-layer and 06–16 MLT for the E-layer) and in the late evening-morning sector (20–2 MLT) for the F- and E-layer. The F-layer backscatter is enhanced during the winter months whereas the E-layer backscatter is enhanced in the summer months. The detailed descriptions are given in the next subsections.

3.3.1 Daytime F-layer, 8-16 MLT

In general, the F-layer echo occurrence is lower in the summer months and higher in the winter months. January has echo occurrences of approximately 4×10^3 in each MLT/virtual height cell. February has echo occurrences 1.5 times higher compared to January, reaching peaks of 6×10^3. This may be

due to the return of the Sun in mid-February resulting in greater rates of photoionisation and therefore increased electron densities. In March the echo occurrence decreases to values comparable to those encountered in January. This may be due to a blanketing effect in which most of the transmitted signal is reflected in the E-layer before it reaches the F-layer. Backscatter from the E-layer can be caused by photoionisation at lower altitudes. This allows more refraction to occur leading to better propagation conditions enhancing the chances to receive backscatter from the electron density irregularities. The solar radiation is in fact hitting the Earth at higher angles during the spring and summer months allowing photoionisation at lower altitudes.

From April to August the F-layer has very low echo occurrences. One can predict that most likely in the summer the E-layer is refracting a great part of the radiation causing a blanketing effect as mentioned above. In fact the quantity of received backscatter depends on the electron density of the ionosphere since ionospheric backscatter occurs when the radio waves are bent enough to encounter the plasma perpendicularly [*Ruohoniemi et al.*, 1989]. It should be noted that August is a peculiar month. In fact the radar was not transmitting for 15 days, therefore the detected echo occurrence results in lower monthly values.

The blanketing effect observed in the summer months is illustrated using a ray-tracing simulation in Figure 3.2. The model used for the ray tracing was developed by *Coleman* [1998]. In order to find the refractive indices of the ionosphere, a non-collisonal approximation of the Appleton-Hartree equation is used. To model the ionospheric profiles the latest International Reference Ionosphere (IRI-2011) is used. In these plots the bold black lines represent areas where the orthogonality condition needed for good backscatter is satisfied within 1° [*Ponomarenko et al.*, 2009]. The ray tracing is done for year 2016 assuming that the propagation conditions are roughly the same as year 2017. The reason for that is the lack of model data for 2017. The plots in figure 3.2 show the ray tracing for beam 7 for one representative day in January and June.

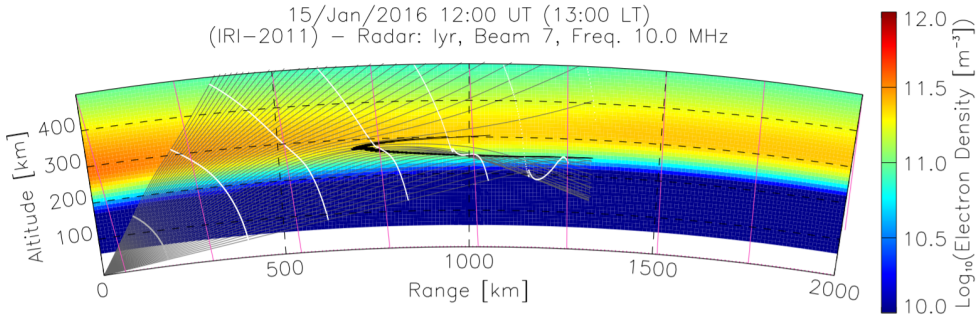

(a) Ray tracing for January 2017

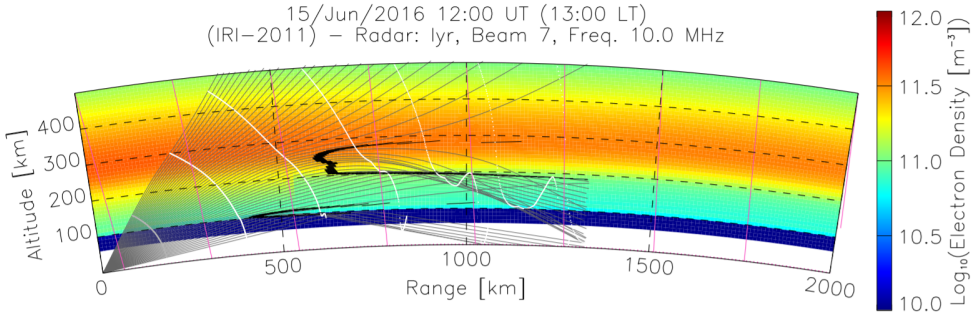

(b) Ray tracing for June 2017

Figure 3.2: (a) Ray tracing for January 2017 and (b) Ray tracing for June 2017

The ray-tracing results indicate that, for January, the backscatter is expected to come from the F-layer and this agrees with the radar data in Figure 3.1. For June the backscatter is expected to come from both the E- and F-layer. The E-layer backscatter is the one causing a blanketing effect. According to this model one should see enhanced backscatter also for the F-layer, however this is not the case according to the Figure 3.1 results. This might be due to reduced occurrence of electron density irregularities, resulting in less backscatter. It should be noted that the ray-tracing model is not completely reliable in the polar regions since there is not so much data used to create the model.

September has a negligible echo occurrence for the dayside F-layer backscatter. However, the backscatter of this month is influenced by the two solar proton events that caused strong attenuation of the radio waves transmitted by

the radar [*Bland et al.*, 2018]. October is also an anomalous month and presents very high values of echo occurrences. The reason for this high echo occurrence may be due to very good ionospheric propagation conditions. November and December have echo occurrences comparable to January.

3.3.2 Late evening-early morning F-layer, 20-02 MLT

In the 20–2 MLT sector, the F-layer echo occurrence for Janury to March are approximately 3×10^3. The echo occurrence is reduced compared to the daytime. During the summer months echo occurrence is very low at these times. However, in June and July there is some backscatter coming from the lower F-layer. September doesn't follow the trend for the reason mentioned above. October, as stated above, is an anomalous month and presents higher values of echo occurrence compared to the other months and a prolonged detection period. In fact, the late evening detection starts at 16 MLT and lasts until early morning 03 MLT. November has values comparable to those encountered in January. December has echo occurrences values only for the late evening sector.

3.3.3 Daytime E-layer, 6-16 MLT

The echo occurrence for the E-layer increases in the summer and decreases in the winter for the reasons above mentioned. The period of time in which the E-layer is observable is shifted towards the early morning sector for February, March and October.

3.3.4 Late evening-early morning E-layer, 17 mlt-02 mlt

In January, October, November and December the late evening sector shows echo occurrences of approximately 3×10^3, which is greater than the other months. The time period at which the backscatter is detected starts approximately at 17 MLT. In order to clearly show this phenomenon, the same plot is reproduced in a logarithmic scale for January, as a month to represent the behavior in the winter, to enhance features that cannot be seen strongly with the linear colour scale used in Figure 3.1.

*L*YR backscatter properties

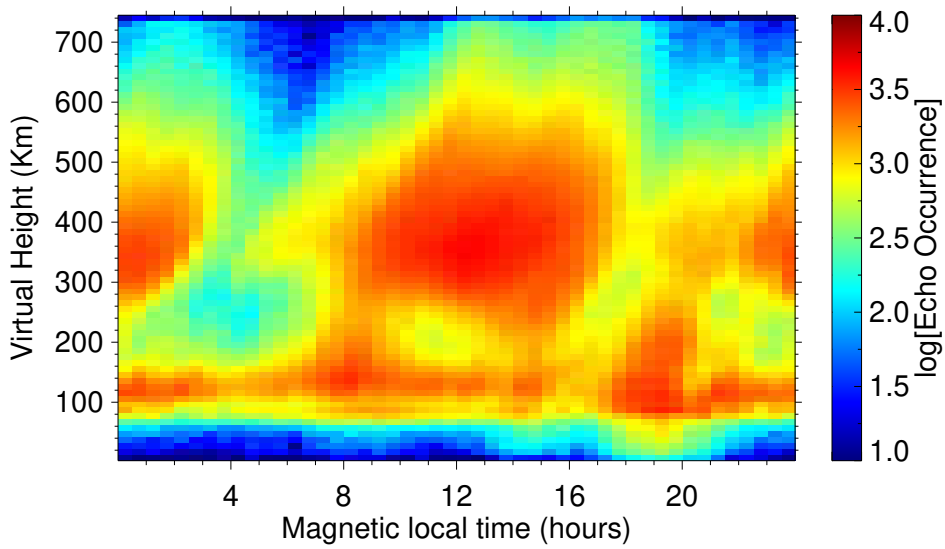

Figure 3.3: Logarithmic plot for the echo occurrence over virtual height and MLT for January 2017.

It is possible from figure 3.3 to observe significant echo occurrence at very low virtual heights (50–60 km) between 17 MLT and 22 MLT. This phenomenon might be associated with substorm activity leading to increased particle precipitation. Increased particle precipitation may contribute to higher levels of ionisation. This causes more refraction to occur leading to better propagation conditions and enhancing the backscatter signal for this period of time.

To determine whether substorm activity is indeed responsible for the increased echo occurrence in this sector, the magnetometer data from Longyearbyen were used to estimate the number of substorms in January. A total of 17 substorms occurred, which were characterized by sharp narrow peaks with an intense decrease of the H component of the geomagnetic field measured at the Longyearbyen station.

In order to further illustrate this phenomenon, figure 3.4 shows the plots for the radar backscatter power, the magnetogram and the keogram for 1 January 2017. The radar backscatter power is represented as a function of slant range and UT time, the H component of the geomagnetic field is displayed using a

magnetogram and the keogram shows scan angle in degrees over UT time. To correlate the slant range with the virtual heights the model by *Chisham et al.* [2008] has been used. The E-layer is defined below 600 km slant range. Echoes from ranges below 250 km are attributed here to substorm activity.

The first substorm occurs approximately at 17:30 UT and corresponds to a sharp decrease in geomagnetic field intensity. However, in the radar data the backscatter power is not elevated. This might be due to the fact that the radar signal was absorbed by the substorm. The second substorm occur at approximately 18 UT and corresponds to elevated backscatter power and a lower sharp decrease in geomagnetic field compared to the first substorm. These events are shown as well in the all sky camera data with increased 557.7 nm wavelengths auroral emissions.

The time offset between MLT time and UT time corresponds to approximately three hours when considering the location the E-layer backscatter. Short slant ranges are typical for the E-layer backscatter due to the half hop propagation mode. Therefore 17 MLT corresponds to approximately 14 UT and 22 MLT corresponds to approximately 19 UT.

From February to September the echo occurrences for the late evening sector are very low. The low echo occurrence for the summer months is also supported by magnetometer data. Substorms were counted for the month of June between 17 and 22 MLT to make a comparison with January and the amount registered in June was half the amount recorded in January. This shows evidence of reduced substorm activity in the summer months. Substorm activity is enhanced during the winter due to a seasonal effect related to the Earth's tilt [*Tanskanen et al.*, 2011]. The Earth's tilted axis of 25.5° results in the distance along the magnetic field lines between the pole and the average reconnection point in the magnetotail being shorter in the winter compared to the summer. This leads to a large summer-winter asymmetry in the number of substorms. This is because the shape and behaviors of the magnetotail and the reconnection processes are dominated by solar influences. The different distances give rise to two different consequences. The electric charges accelerated at the average reconnection point follow mainly the shortest path, strengthening

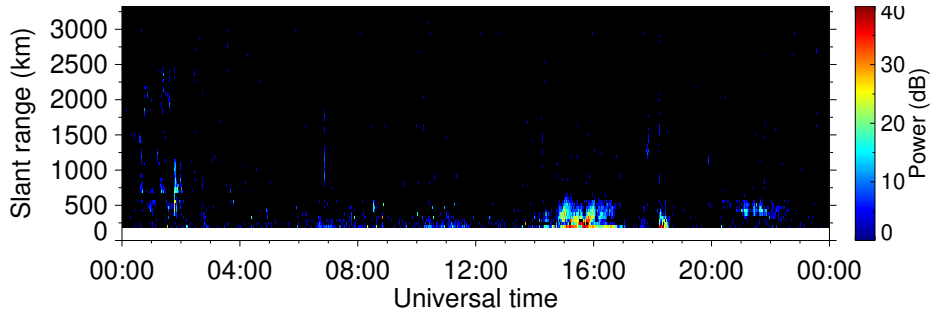

(a) Radar backscatter power

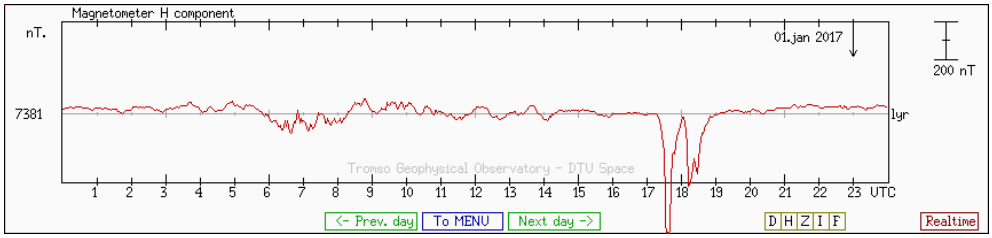

(b) Magnetogram

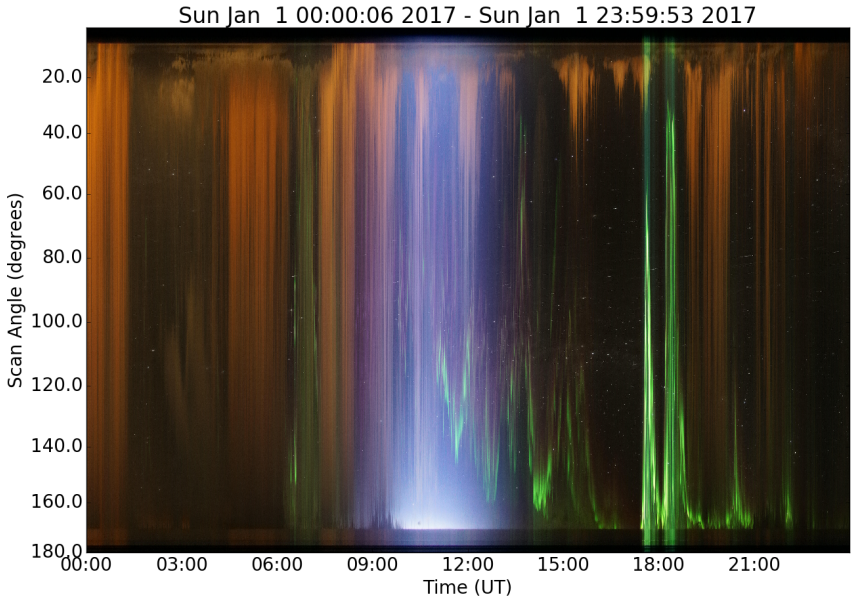

Figure 3.4: (a) Lyr SuperDARN radar backscatter power (b) Magnetogram for the Longyearbyen magnetometer and c) Keogram for 1 January 2017.

substorm precipitation in the winter. In the summer, the energy carried by the charges that follow the longer path is damped much more compared to the winter due to the longer distance they have to travel. Therefore, they don't have enough energy to precipitate or, if they have enough energy to precipitate, they don't have enough of it to reach low altitudes. This results in very low or absent echo occurrence of late evening precipitation in February, March and the summer months. Some traces of backscatter in the early morning sector are noticeable in January, September, October and December.

3.3.5 Statistics for year 2018

Overall, there is a smooth transition in the echo occurrences of the E-layer and the F-layer between winter and summer months, both during the day and during the late evening-early morning sector in 2017.

The same statistics are reproduced for year 2018 to investigate if the events in August and September have an impact on the conclusions that can be drawn for year 2017. August and September follow the trend of year 2017 with a decrease (increase) in echo occurrences for the E- (F-) layer. October 2018 presents values that follow the trend, with a smooth transition and not so high echo occurrence values. Therefore, this supports the theory that the conditions in October 2017 were exceptional for radio-wave propagation leading to high values of detected backscatter. It should be noted that the results for the two different years are compared looking at 22 days of backscatter since the Longyearbyen radar stopped being operational after the 23 October.

3.3.6 General observation on the E-layer backscatter signature

The E-layer backscatter appears to be divided into two populations for April, May, June, July and August. This is unexpected because backscatter from this layers would give rise to a continuous distribution of virtual heights. In fact, the two layers are physically very close to each other and the radar cannot resolve the distances between the two layers (see Figure 1.5). However, the two different regions could arise from errors in the elevation angles as seen in subsection 2.1.4 [*McDonald et al.*, 2013; *Milan et al.*, 1997].

3.4 Ionospheric electron densities associated with the F and E ionospheric layers

Figure 3.5 shows the histograms of electron density for the E- and F-layer scatter in January and June. These months are chosen to best represent the winter and the summer trends respectively. In the winter there is an enhancement of echo occurrence for the F-layer whereas in the the summer there is an enhancement of echo occurrence for the E-layer. Electron densities are divided into two populations, below 140 km for the E-layer and above 140 km for the F-layer, according to *Bland et al.* [2014]. The electron densities are calculated with equation 1.13. As mentioned in section 1.5.4 the method used has limitations regarding the electron densities due to using an approximated form of the Appleton-Hartree equation.

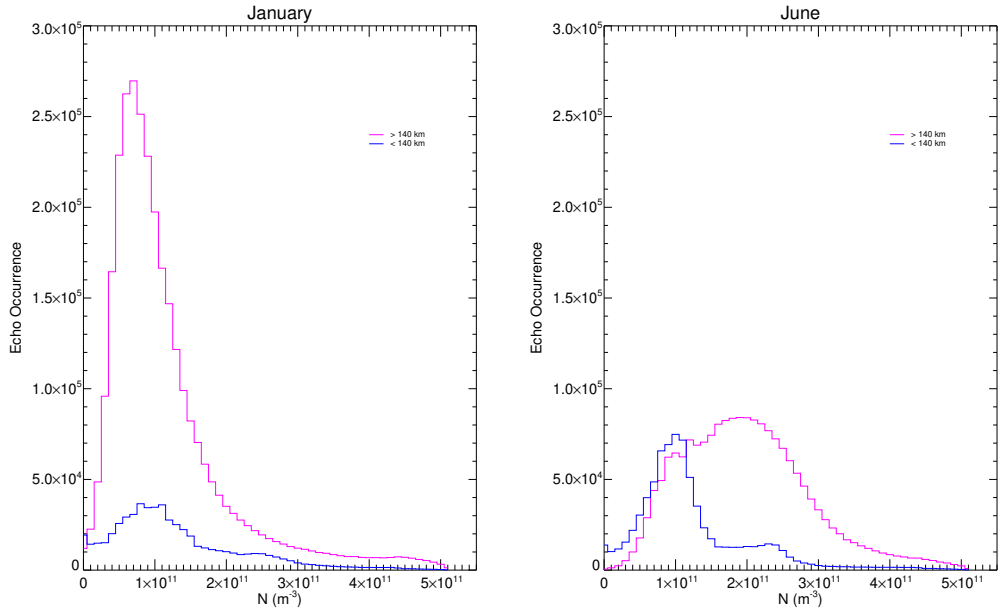

(a) January (b) June

Figure 3.5: Histograms of E- and F-layer electron densities for (a) January and (b) June.

During the summer, higher densities are found for the F-layer compared to

the ones found in the winter. Densities in the summer have approximately double the values, around 2×10^{11} m^{-3}, compared to the values encountered for the winter, around 1×10^{11} m^{-3}. This behavior and the peak values for the densities are similar to those found by *Koustov et al.* [2018]. The F-layer in the summer has greater densities than the E-layer. This is expected because the F-layer is more ionised than the E-layer since it receives more solar radiation that causes photoionisation. For the winter the densities of the F- and E-layer are about the same values. This is not expected since the F-layer densities are usually found to have higher values compared to the E-layer densities. This result might be caused by limitations of the *Gillies et al.* [2009] method when the ionosphere is very weak. Another reason could be the absence of solar radiation. This is causing reduced photoionisation rates in the ionosphere resulting in the observation of similar densities for the two different virtual height regions. The only difference is therefore a much greater echo occurrence for the F-layer. This difference can be attributed to the larger amount of ionospheric plasma detected in the F-layer compared to the E-layer. Possibly this might be due to the fact that the F-layer covers a broader area. Another interesting aspect is that the F-layer for the summer and the E-layer for the winter show a spread peak rather than a sharp peak. This spread peak feature is most likely due to a greater range of electron densities within these layer. Sharper peaks in the plots would correlate to a smaller range of electron densities within the ionospheric layer. Sharp peaks could also be a sign of preferential detection of a small range of densities, while the reverse could be said for spread peaks. This preferential detection could be related to better scattering conditions or better conditions for the formation of irregularities.

Moreover, there is a "lump" in the high-density tail of each distribution shown in Figure 3.5. This is a consequence of the behavior found for the distributions of the elevation angles. The histograms, in figure 3.6, of the elevation angles for January and June are reported to illustrate this effect.

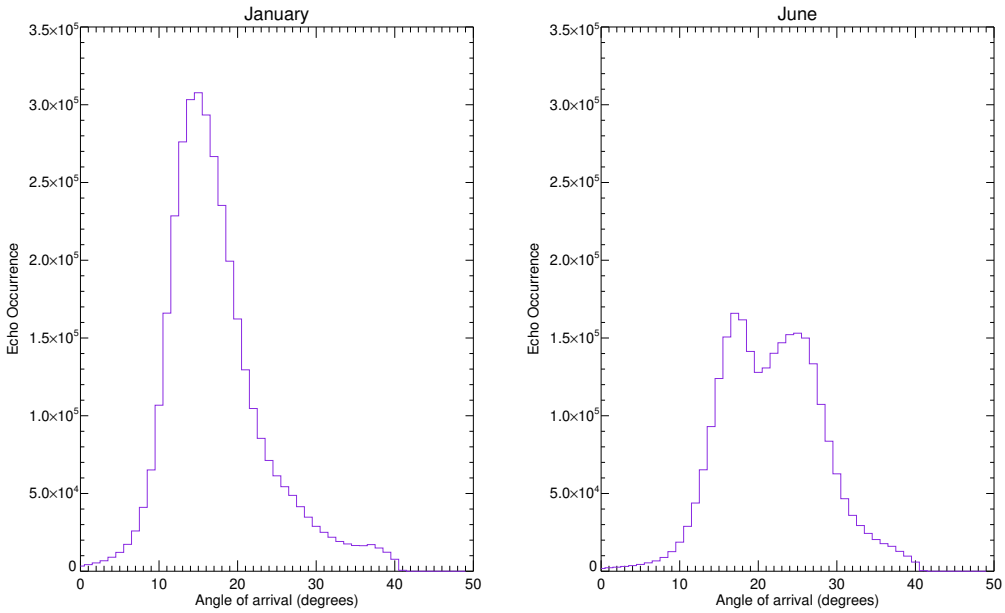

(a) January (b) June

Figure 3.6: Histograms of the elevation angles for (a) January and (b) June.

It is possible to observe a "lump" in January for high elevation angles (above 30°). For June there are two peaks in the echo occurrence related to 15° and 25°. This behavior might be due to the aliasing effect of the elevation angles mentioned above.

It should be noted that the approximated form of the Appleton-Hartree equation has a degree of error for the refractive index. This cannot be corrected with the current understanding and measurements. This then leads to an error within the values obtained for the electron density at the point of reflection.

3.5 Magnetic local time (MLT) and magnetic latitude (MLAT) for the echo occurrence

Figure 3.7 shows the echo occurrence over time and magnetic latitudes for all months in 2017. Most of the backscatter originates from magnetic latitudes between 75° and 84° as one can expect due to the location of the radar facing towards north-east. Also, the $\frac{1}{2}$-hop propagation mode is more likely to occur since the ionosphere over Svalbard is too weak to routinely support 1-hop and 1-$\frac{1}{2}$-hop, which places most of the backscatter in the 75 −-84° latitude range.

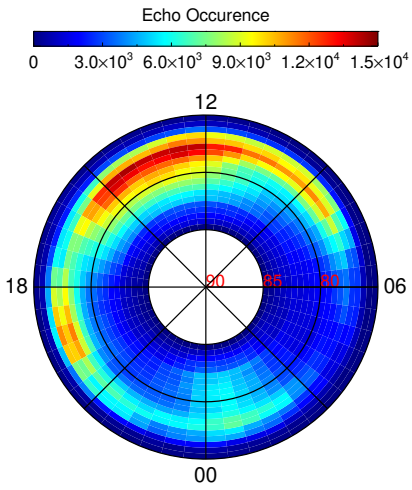

(a) January

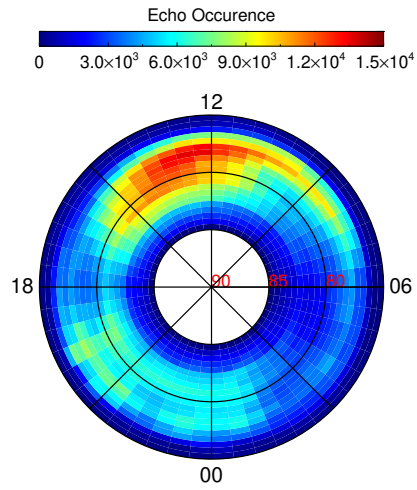

(b) February

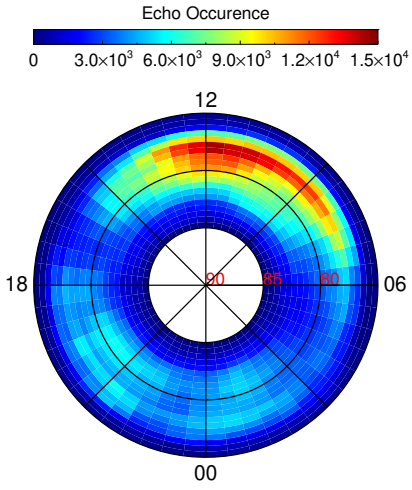

(c) March

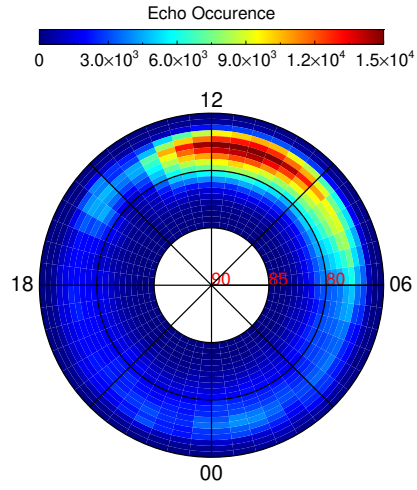

(d) April

Figure 3.7: Polar plots for echo occurrences versus magnetic local time and magnetic latitude for year 2017.

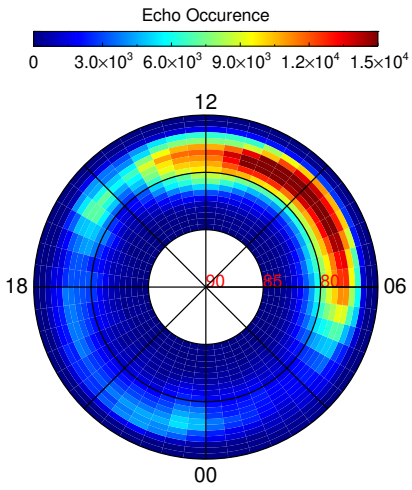

(e) May

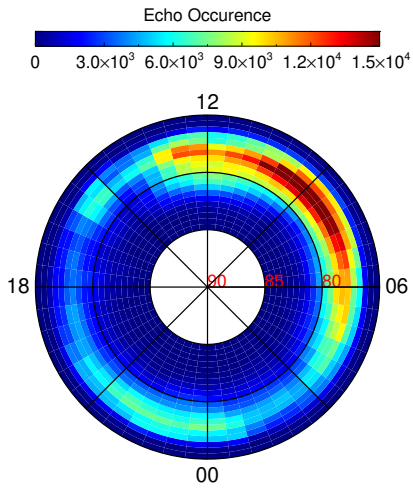

(f) June

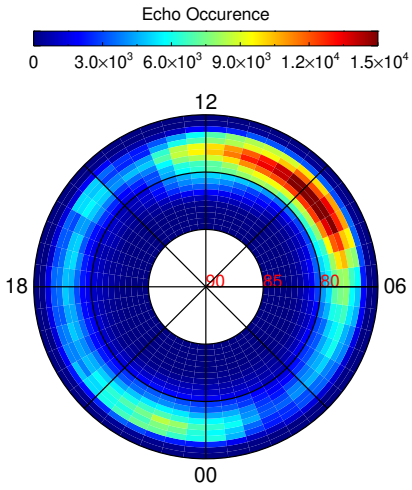

(g) July

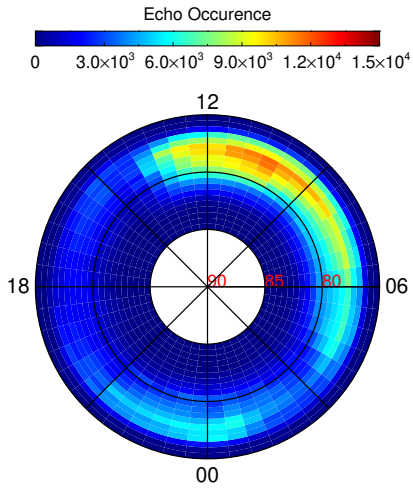

(h) August

Figure 3.7: Polar plots for echo occurrences versus magnetic local time and magnetic latitude for year 2017.

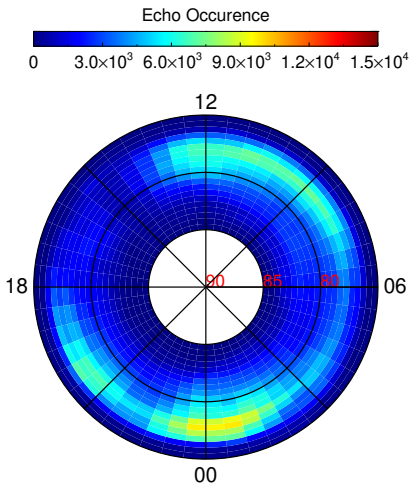

(i) September

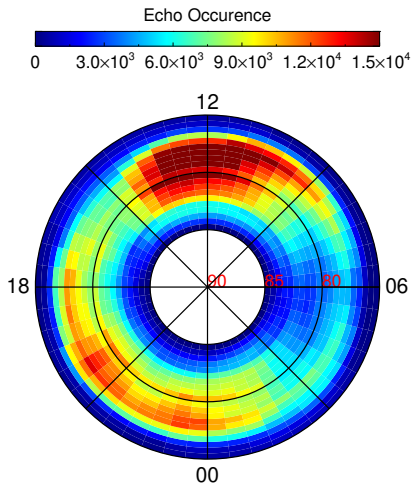

(j) October

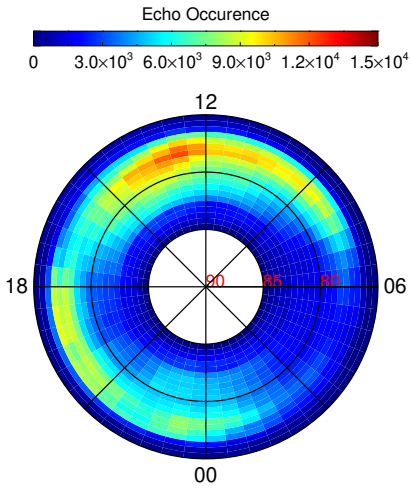

(k) November

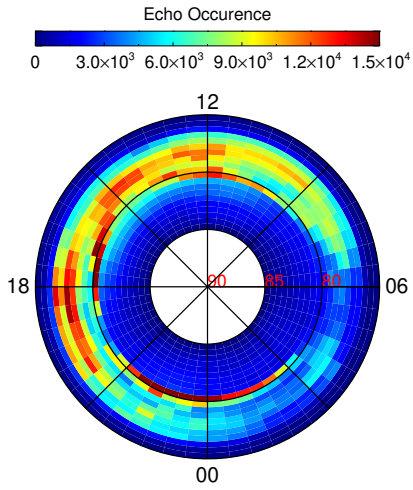

(l) December

Figure 3.7: Polar plots for echo occurrences versus magnetic local time and magnetic latitude for year 2017.

Data below 75° were excluded since the echo occurrence for the plasma at these latitudes is too low to give a reliable overview of the ionospheric behavior in that region.

A defined area of high echo occurrence between is observed in January be-

tween 16–12 MLT. Proceeding from winter to summer the backscatter echoes appear to be at a lower MLT area, between 12–6 MLT. In August the high echo occurrence area appears at greater MLTs and in November the backscatter echoes have high intensity between 12–16 MLT. In September the echo occurrence is decreased overall due to the two solar proton events occurring in this month. This event caused HF radio attenuation and that is the reason why there is not a significant amount of detected backscatter. The data was analysed for this month for year 2018 and the trend is in accordance with what was observed from winter to summer for 2017. May, June and July have higher echo occurrence than the previous months with values very close to the maximum echo occurrence value of 1.5×10^4. This is presumably due to the fact that during these months ionisation rates are elevated due to increased photoionisation. For April, May, June and July the area of high echo occurrence is narrowed to 5–6° of latitude. The defined area is increased in size and intensity for October while December appears anomalous and shows no clear areas of consistent enhancement.

Another defined region of increased echo occurrence is shown between 18–0 MLT for January and February. This region becomes insignificant in March, April and May and appears to be at higher MLTs until September where it has increased echo occurrence after midnight. In October and November this region appears to be in the same location assumed in January, however the highest echo occurrence is observed in January and October.

In this chapter the echo occurrence was studied as a function of virtual heights and MLT and MLAT for the different months. In chapter 4 velocities and spectral widths are investigated and related to the physical processes of the ionosphere-magnetosphere system.

Chapter 4

Ionospheric convection and cusp signatures

Presented in this chapter is an analysis of the average doppler velocities and spectral widths measured by the LYR radar. The results of this analysis are used to identify key features of the polar ionospheric dynamics and structure, including the local convection patterns, the radar signature of the cusp and whether the LYR radar can detect polar cap patches.

4.1 Method

The LYR data for each month were divided into bins of 0.5 MLT and 0.5° MLAT. In each bin, the average velocity and the average spectral width were determined. Since the velocity is a vector quantity, the absolute value of the velocity was used when calculating the average.

The radar data were also sorted according to IMF conditions. The IMF data were taken from the DSCOVR satellite. The data were one minute averaged for B_x, B_y and B_z in GSE coordinates. In order to correlate the radar data with IMF conditions, the IMF data has been shifted by one hour. It is assumed that approximately an hour is the time delay between the IMF measurements taken at L1 lagrangian point and the time at which the IMF have an effect on

the polar ionosphere.

4.2 Ionospheric convection

One of the primary objectives of SuperDARN is to measure ionospheric convection [*Chisham et al.*, 2007]. The relationship between IMF and convection patterns was investigated by early SuperDARN studies. *Ruohoniemi and Greenwald* [1995] showed that both IMF B_y and season affect the ionospheric patterns in the nightside flow.

However, the nightside behavior, 6–18 MLT, is not discussed in this thesis. This is because the IMF conditions take longer than an hour, the time shift used, to affect the magnetotail. There is also an uncertainty on the time at which the effects are observed in the ionosphere.

4.2.1 Velocity features

Figure 4.1 shows polar plots of averaged velocities over magnetic local time and magnetic latitude for March and June. March and June are used as representative months in order to show the seasonal trend encountered in the velocity features in 2017. Key features of the data are identified as regions A, B, D, E. The features in March are typical of months between September and March where the positions and velocities of region A and region D vary to some degree but not significantly. The features seen in June are typical of the months from May to August where the size of region E and the velocities recorded vary but not substantially.

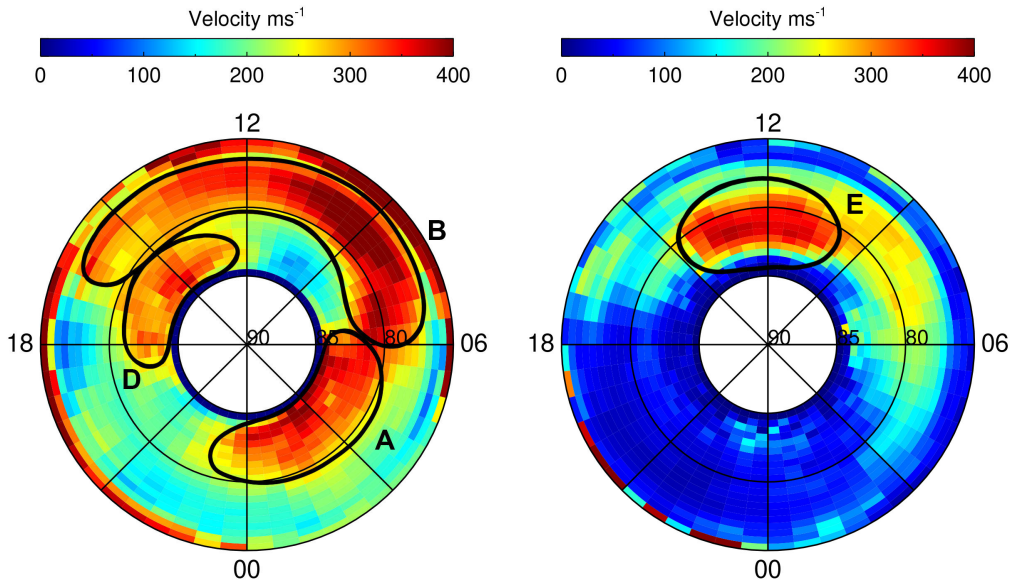

(a) March (b) June

Figure 4.1: Polar plots of the average velocity over magnetic local time and magnetic latitude for March and June.

The averaged parameters are physically reliable only in bins with high echo occurrence. Therefore, data below 75° were excluded due to low echo occurrence (see Figure 3.7). Between 84.5° and 85° there are no radar data due to the radar field-of-view.

In March there is a high velocity feature above 80° between approximately 0–6 MLT. This is denoted by region A. Higher velocities are found approximately between 6–16 MLT below 80° with values of approximately 250–300 m s^{-1} with peaks reaching values of approximately 350–400 m s^{-1} between 6–12 MLT. This is denoted by region B. The region at higher latitudes above 80° between 12–19 MLT is denoted by region D and the velocities have values of approximately 250–300 m s^{-1} with some values exceeding to 350 m s^{-1}.

In June the peak of high velocity is found between 9 and 15 MLT above 80° with velocities between 300 m s^{-1} and 350 m s^{-1}. This is denoted by region E

in the plot.

Due to the location of the LYR SuperDARN under the dayside auroral oval, it is possible to assume that these regions, seen in March and the months it represents, are associated with convection patterns. Regions A and D are regions of low echo occurrence whereas region B has high echo occurrence. For the region of low echo occurrence, the velocities are also elevated. Therefore, the radar is detecting ionospheric convection but the targets are sporadic and not persistent. Moreover, the targets are smaller and short lived compared to region B. This might suggest the presence of polar cap patches. They are a good scattering target due to their high electron density, therefore they can scatter and be a good tracer to understand the ionospheric flow. The reason why the echo occurrence in this region is low might be due to the fact that the patches are not always present [*Hosokawa et al.*, 2006; *Oksavik et al.*, 2006]. Polar cap patches are investigated further in subsection 4.2.3.

The velocities for regions A, B and D have lower values for June compared to March. Region E is related to cusp signatures and is discussed further in section 4.3.

The blanketing effect mentioned in subsection 3.3.1 reduces F- layer detection for region B [*Ruohoniemi and Greenwald*, 2005]. This leads to a preference in the E-layer detection (see Figure 3.1) and the lower doppler velocities measured may be typical of the E-layer of the polar ionosphere. However, ionospheric convection patterns are best measured in the F-layer of the ionosphere [*Chisham et al.*, 2007] therefore the ionospheric convection for June is less evident than March.

4.2.2 IMF conditions

To further investigate the velocity features shown in Figure 4.1, the data were sorted according to IMF conditions. Figure 4.2 shows the dependence of the convection patterns on IMF B_y and B_z for March. March is once again used as a representative month for the IMF B_y and B_z dependent features observed from September to March. Figure 4.3 shows the velocity data for June sorted by IMF B_y^+, B_y^-, B_z^+ and B_z^-.

*L*YR backscatter properties

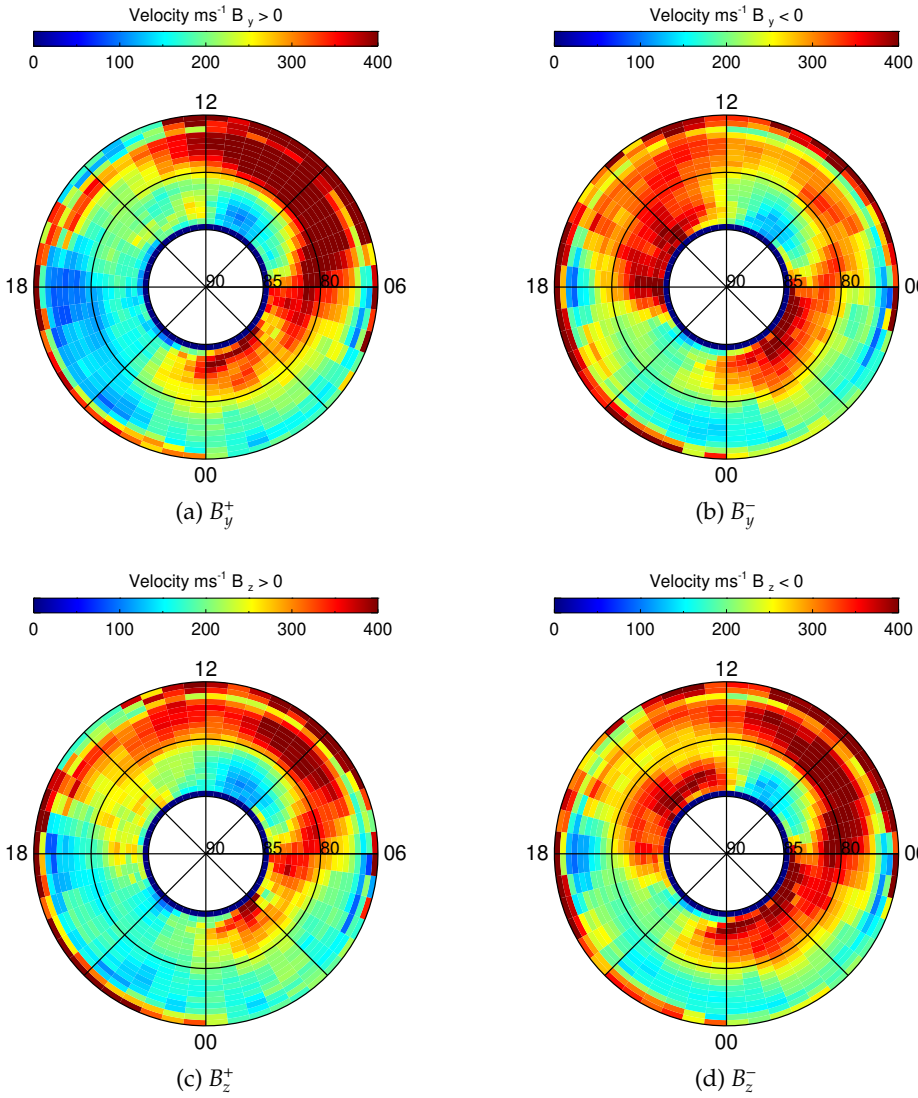

Figure 4.2: Polar plots of the average velocity over magnetic local time and magnetic latitude for March sorted by a) B_y^+ b) B_y^- c) B_z^+ d) B_z^-.

In March the highest velocities occur under B_y^+ conditions. For B_y^- the convection pattern observed in region B is shifted towards higher MLTs.

For B_z^- there is a velocity enhancement in region D and no enhancement for B_z^+. This behavior is investigated in subsection 4.2.3.

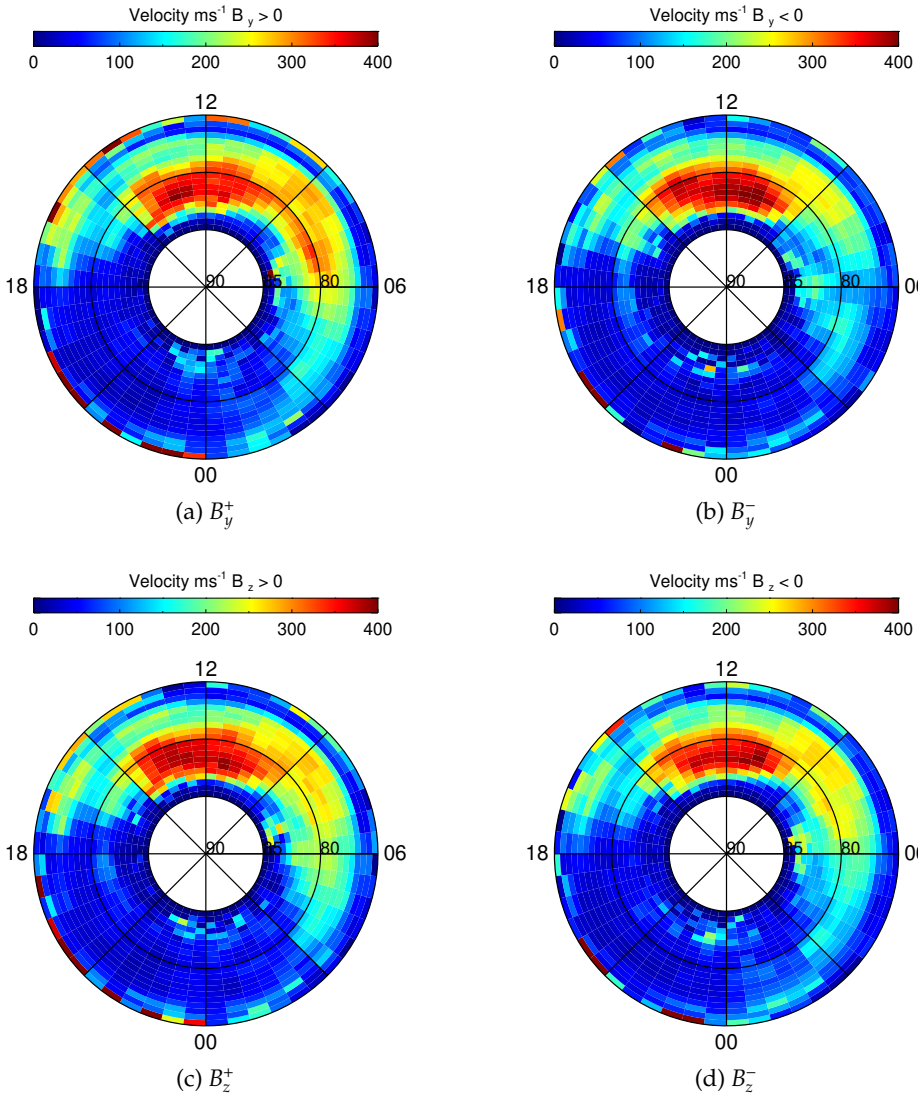

(a) B_y^+ (b) B_y^-

(c) B_z^+ (d) B_z^-

Figure 4.3: Polar plots of the average velocity over magnetic local time and magnetic latitude for June sorted by a) B_y^+ b) B_y^- c) B_z^+ d) B_z^-.

June is used as a representative month for the IMF B_y dependent features observed between May and August. Under the condition of B_y^+ there is some evidence of a region B in the 6-12 MLT sector. The position of these high velocity values agrees with the trend seen within March. Region E sees very

little changes due to a variation in By. This indicates that this feature of the convection is not dependent on B_y.

IMF conditions, in terms of By and Bz, are seen to have no impact on the velocities during June and the months it represents. This is further evidence that there is a blanketing affect creating limitations in the LYR SuperDARN radar's detection of ionospheric convection patterns from May until August.

4.2.3 Polar cap patches

Above 80° MLAT the backscatter measured by the radar is most likely due to an enhancement of polar cap irregularities, referred to as polar cap patches, identified as regions A and D in Figure 4.1. Polar cap patches are patches of high electron density surrounded by significantly lower density plasma making them a good scattering target [*Oksavik et al.*, 2006]. This, combined with their antisunward motion with the convection, makes them a good tracer for understanding ionospheric flows. The formation of patches generally coincides with periods of southward IMF and Figure 4.2 shows higher velocities for region D under southward IMF conditions. This suggests that the radar is detecting patches moving with high velocity flows across the polar cap.

The time period 18–22 UT on 14 November 2017 was chosen for a case study of polar cap patches. This time interval was chosen due to the availability of EISCAT data, which will be used to confirm the presence of polar cap patches. The frequency band used for the data analysis for this case study runs between 11.6 MHz–11.7 MHz (Channel B). Channel B is running the common mode, in which the field-of-view is scanned every 1 minute.

The purpose of this case study is to show a possible antisunward flow of polar cap patches, evident in the SuperDARN data, following the ionospheric convection. It is not possible to determine where the patches are formed. To find the patches, area of short lived, high power backscatter echos lasting for a short period of time, are identified. Figure 4.4 shows enhancements of backscattered power starting at 18 UT. These power enhancements arise because the high electron densities in the patches makes them a good scattering target.

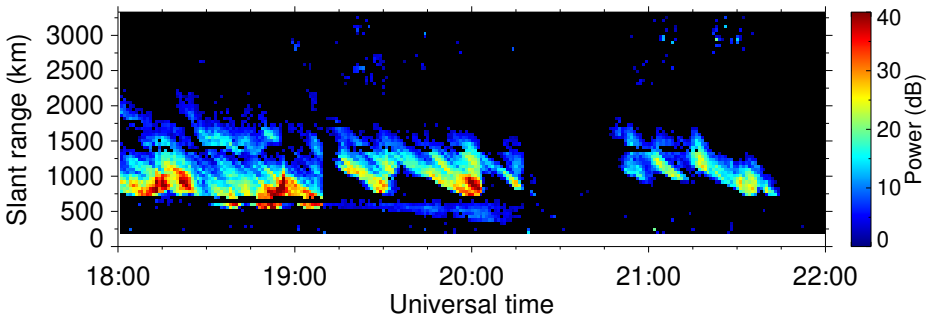

Figure 4.4: Backscatter power over UT time and slant range for 14 November 2017 for channel 2 and beam 2.

In order to see the motion of the patches the backscattered echos are plotted in the radar field-of-view plots. Figure 4.5 shows the field-of-view plots of the radar and the backscattered power for the received echos.

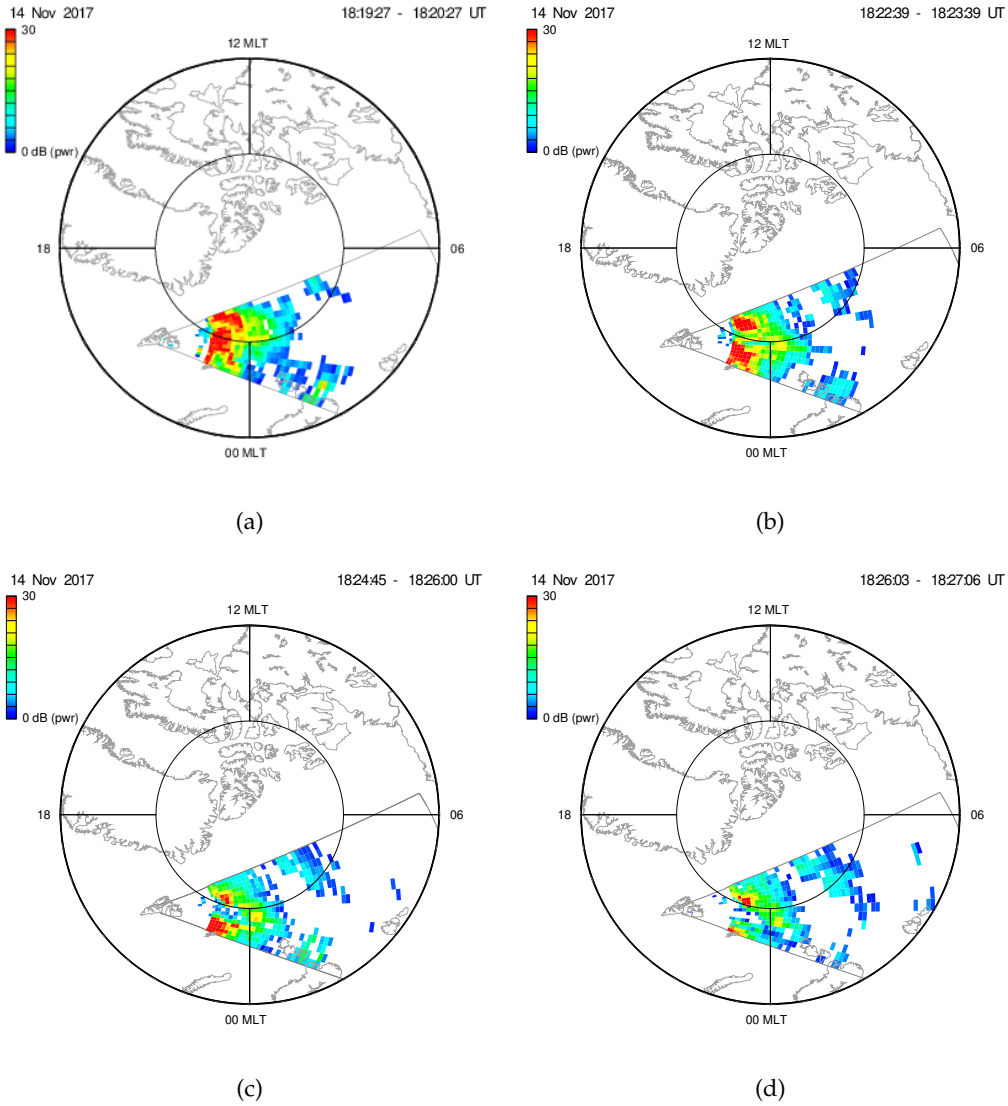

Figure 4.5: Backscattered power in the radar field-of-view.

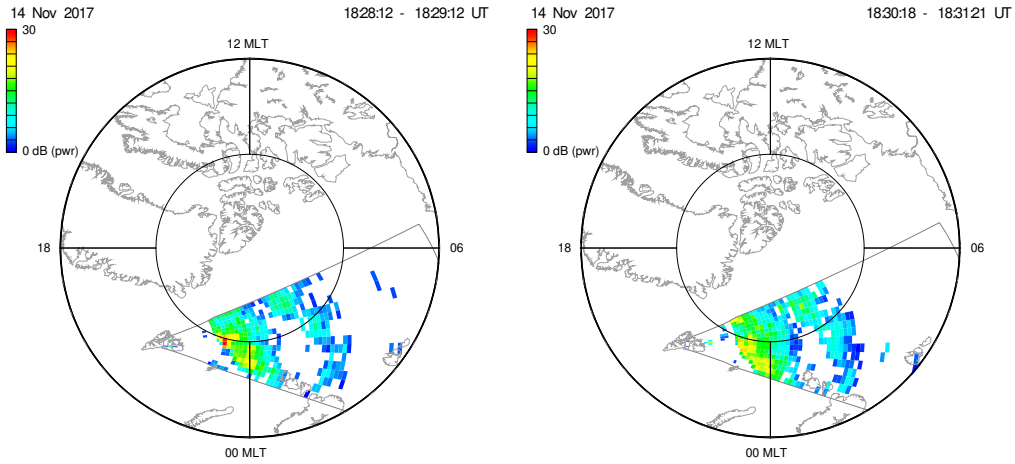

(e) (f)

Figure 4.5: Backscattered power in the radar field-of-view.

There are two patches of high backscatter power at around 18:19 UT corresponding to 21 MLT, moving equatorward. At 21:30 MLT the patches have completely disappeared from the radar field-of-view.

In the same period of time EISCAT radar is showing clear evidence of patches and this is shown in Figure 4.6. Polar cap patches are identifiable in the EISCAT dataset as enhancement in electron density (N_e) and constant electron temperatures (T_e) for all the duration time of the electron density enhancements. It is not possible to say that the patches seen by EISCAT and SuperDARN are the same features because the field-of-view of the two instruments is not overlapping. However, the EISCAT data indicates that patches were present in the premidnight sector during this time period.

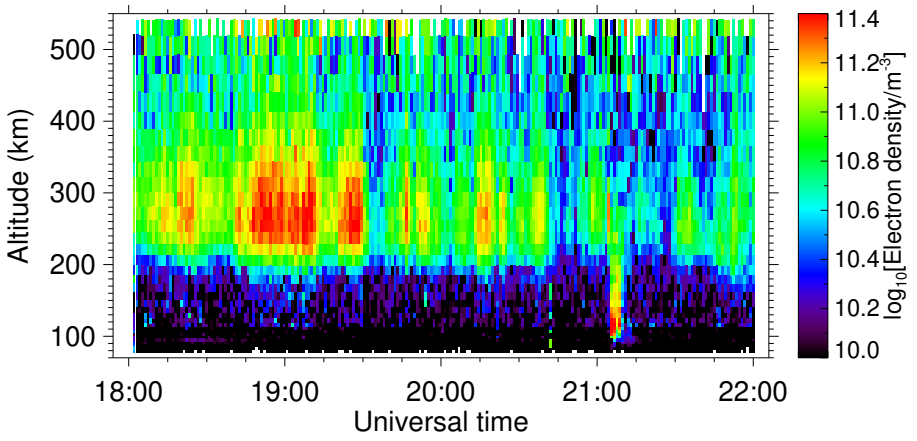

(a)

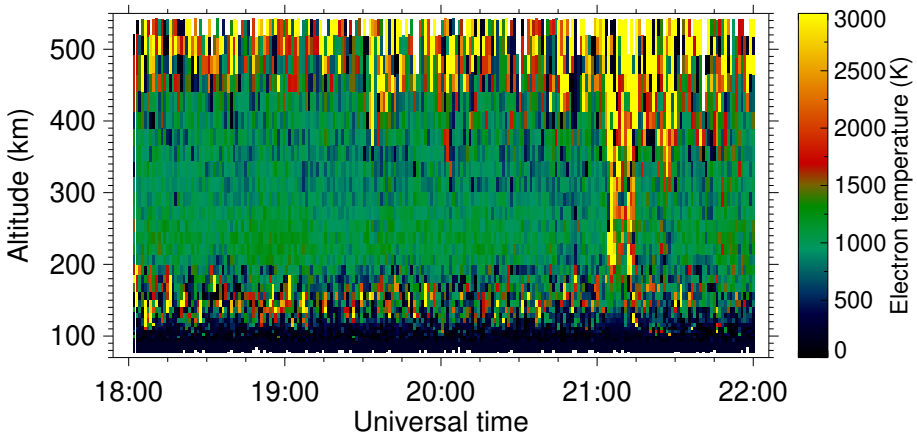

(b)

Figure 4.6: EISCAT radar a) electron density over UT and altitude b) electron temperature over UT and altitude.

4.3 Cusp signatures

In the introduction chapter signatures for radar cusp detection have been discussed. Elevated values of spectral width over a short spatial scale, known as the spectral width boundary, are attributed to the polar cusp boundary. Spectral widths were plotted over MLT and MLAT for each month to find

signatures of regular cusp detection in the Longyearbyen SuperDARN radar. There is a clear seasonal variation in the spectral width data, therefore the two months, January and June, are used to represent September-February and May-August respectively. Figure 4.7 shows the polar plots of the spectral widths over magnetic local time and magnetic latitude for January and June 2017.

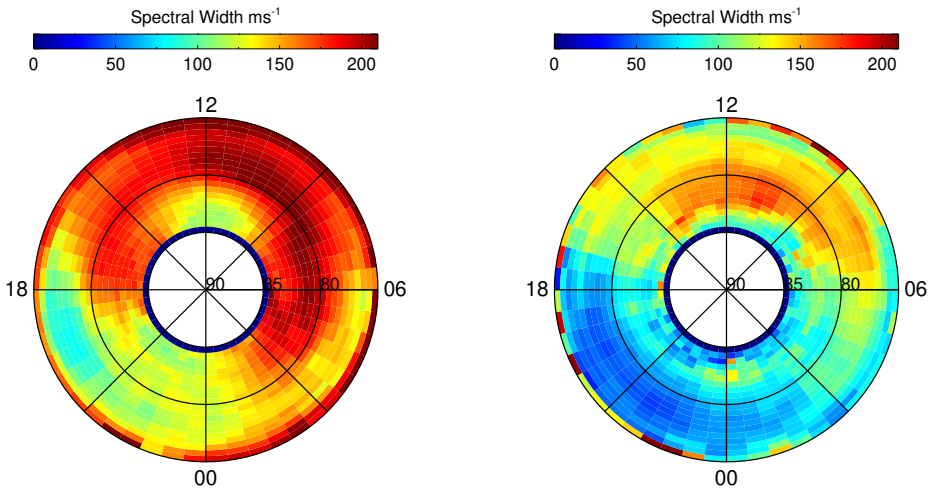

(a) January (b) June

Figure 4.7: Polar plots of the spectral width over magnetic local time and magnetic latitude for January and June.

In January there are large spectral widths that are generally associated with the large velocities of regions A, B and D specified in the velocity plots discussed in section 4.2. There is no clear cusp detection in January and in the months it represents.

In June there is a small region of elevated spectral width that appear to correlate to the region E in the velocity plots discussed in section 4.2.

4.3.1 IMF dependence of the cusp

As discussed in the introduction chapter, the position of the cusp has an MLT variation due to changes in By and latitudinal variations due to changes in Bz.

*L*YR backscatter properties

To investigate if the regions of high spectral width in Figure 4.7 are evidence of cusp detection, the spectral width plots are sorted by By and Bz. The same months are used as representative months for the IMF sorted plots. Figure 4.8 and 4.9 shows the polar plots of the spectral widths over MLT and MLAT sorted by IMF conditions.

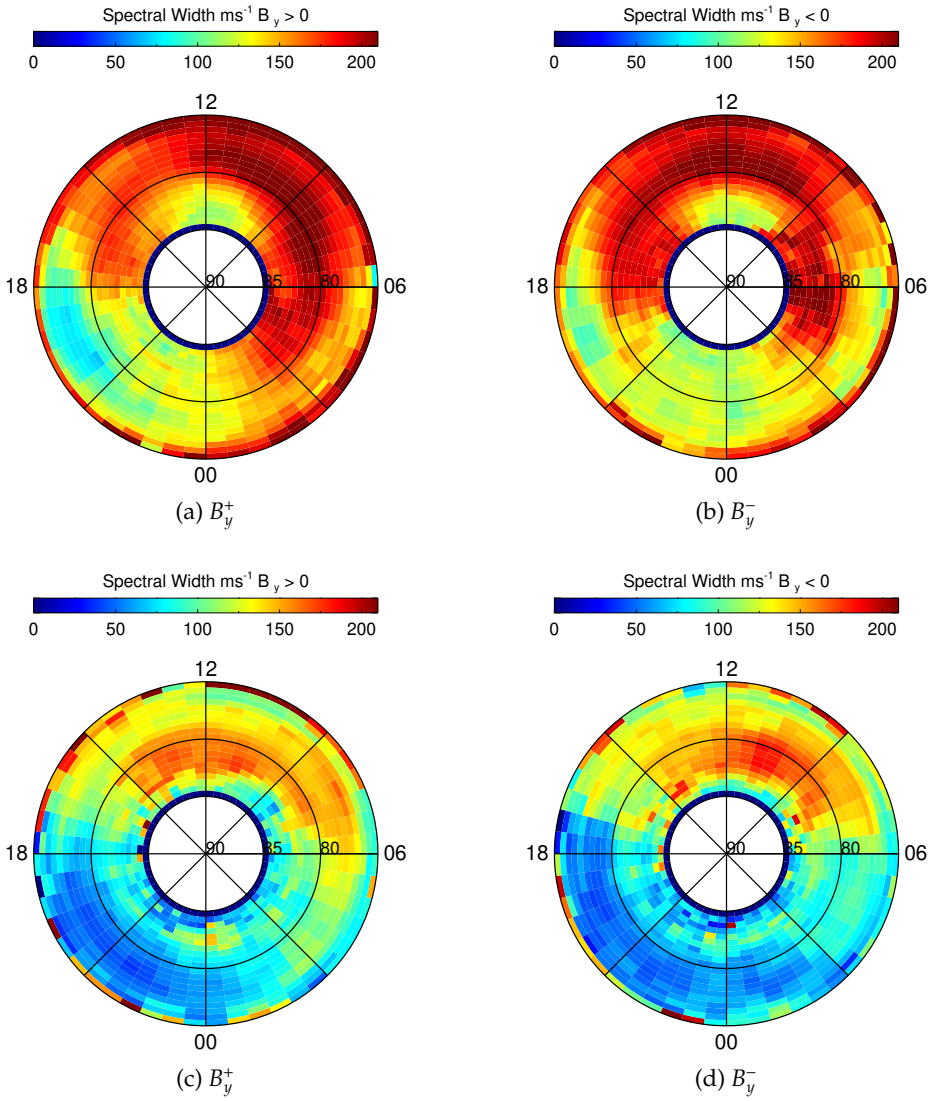

Figure 4.8: Polar plots of the spectral width over magnetic local time and magnetic latitude for January and June for By conditions.

*L*YR backscatter properties

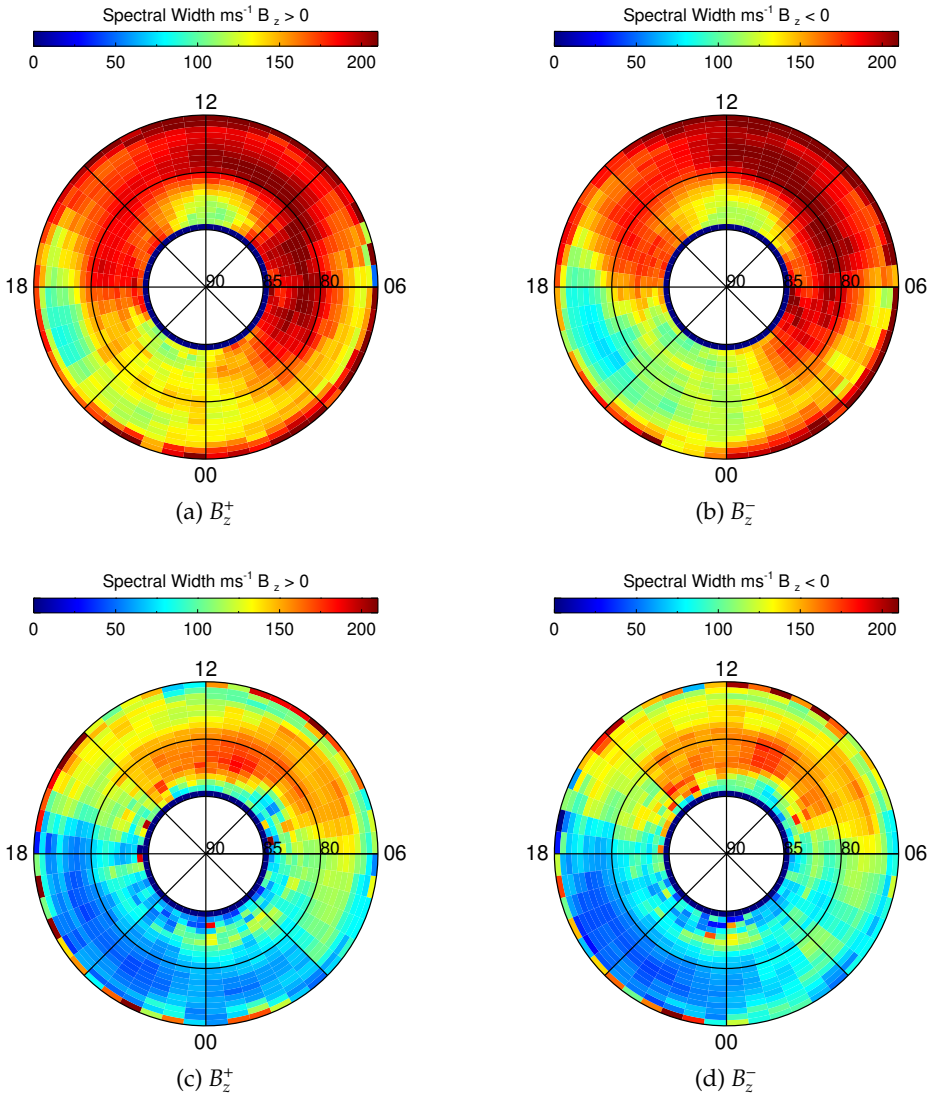

Figure 4.9: Polar plots of the spectral width over magnetic local time and magnetic latitude for January and June for Bz conditions.

From Figure 4.8 and 4.9, unlike the earlier work [e.g. *Sandahl*, 2003; *Pitout et al.*, 2006; *Wing et al.*, 2005] there is no clear evidence of changes of cusp features for B_y^+, B_y^-, B_z^+, B_z^- conditions. However, the detection of the cusp by the Longyearbyen SuperDARN radar appears to be seasonal or it may

suggest a weaker cusp during January and the months it represents. A reason for this could be that the ionospheric convection is predominant in the winter obscuring cusp detection.

Chapter 5

Summary and Conclusion

Presented in this chapter is an overview of the different features observed with the LYR SuperDARN.

In chapter 3 the echo occurrence was studied as a function of virtual heights and MLT and MLAT for the different months. The monthly plots in Figure 3.1 have shown that there is a seasonal change in the detection of the E- and F-layer of the ionosphere, in terms of echo occurrence during daytime and late evening-early morning. In particular, increased echo occurrence for the F-layer during daytime is characteristic of the winter months whereas the enhanced echo occurrence for the E-layer is characteristic for the summer months. The seasonal variation in echo occurrence for the two ionospheric layers has been attributed to a blanketing effect. A ray-tracing simulation showed that the E-layer is causing refraction of the HF radio waves leading to enhanced backscatter from the E-layer and reduced backscatter from the F-layer.

The late evening-morning sector has very low echo occurrence compared to the winter months. The higher winter echo occurrences observed for January, October, November and December are attributed to particle precipitation events, especially substorm activity. This was supported by magnetometer data as well confirming that more substorm events occur in the winter rather than in the summer. It was pointed out that substorm activity is enhanced

during the winter due to a seasonal effect related to the Earth's tilt. This is one piece of evidence of asymmetries between the northern and southern hemisphere.

Ionospheric electron densities were also investigated. In the summer the F-layer electron density is double that of the winter and this was expected since the summer F-layer is subject to both photoionisation and particle precipitation. In the winter, electron densities for the E- and F-layer were similar. This is because it is possible for the E-layer backscatter to be detected without satisfying the orthogonality condition [*Milan et al.*, 2004]. This suggests that the E-layer electron densities calculated using the method described by *Gillies et al.* [2009] are probably not reliable in the wintertime. Moreover, it could be related to absence of solar radiation which is causing reduced photoionisation rates leading to similar electron densities for the two different ionospheric layers. It was also found that the F-layer in the summer and the E-layer in the winter have spread peaks in the electron density distribution. This is associated with a greater range of electron densities for the two ionospheric layers. Whereas, sharp peaks are a sign of preferential detection of a small range of densities due to better scattering conditions or better conditions for the formation of irregularities. It was also shown that for the month of June the overall echo occurrence for the E-layer is lower than the F-layer. This is due to the fact that the F-layer covers a larger detection area for the backscatter targets. However, the comparison between the two months was enough to understand that the echo occurrence for the F-layer in the summer is much less than for the winter.

In chapter 4, velocities and spectral widths are investigated and related to the physical processes of the ionosphere-magnetosphere system. It was possible to see features of the local convection patterns, especially enhanced velocities in the dayside auroral oval. The seasonal variation found for the ionospheric flow is evidence that the blanketing effect is obscuring the convection flow during the summer. To support this statement is also the fact that the IMF conditions have no impacts on the velocity features in the summer.

Within the convection flow it was possible to study the motion of polar cap

patches in the polar ionosphere. Polar cap patches are a good tracer to study the ionospheric convection due to their high electron densities making them a good scattering target.

It was also possible to attribute the dayside high spectral widths to cusp detection. However, the variations in MLT and MLAT found by previous studies [e.g. *Sandahl*, 2003; *Pitout et al.*, 2006; *Wing et al.*, 2005] under IMF B_y and B_z conditions were not supported by this study. Moreover, it was possible to assess that the detection of the cusp by the LYR radar is seasonal or the ionospheric convection is predominant in the winter obscuring cusp detection.

5.1 Conclusion

The LYR SuperDARN has demonstrated its capabilities to detect ionospheric convection patterns through the backscatter from ionospheric electron density irregularities. Moreover, it has shown seasonal variations in the polar ionosphere in terms of cusp detection, particle precipitation processes and electron densities. Therefore, it can be said that the LYR SuperDARN radar has the capabilities of detecting the cusp in the northern polar hemisphere and the local ionospheric convection. Moreover, it was possible to detect backscatter from polar cap patches and this was validated using the EISCAT radar. Some limiting factors have however arisen in this study. The elevation angle aliasing effect caused ambiguity in electron density measurements. The blanketing effect was believed to cause a seasonal effect on the detection of ionospheric convection patterns making it harder to observe the dayside convection in the summer. Some research could be done to reduce these effects and improve the capabilities of SuperDARN measurements. Moreover, some further research could be done regarding the influence of the IMF conditions on the ionospheric convection and possibly study the nighttime sector in more detail. Further investigations could be done for the cusp region due to the special location of the LYR radar. It may also be possible to isolate the wintertime cusp signatures from the background dayside convection. This would allow the LYR SuperDARN data to be used together with optical data

and rocket experiments during the polar night to study the cusp.

References

Ahn, B.-H., G. Chen, W. Sun, J. Gjerloev, Y. Kamide, J. Sigwarth, and L. Frank (2005), Equatorward expansion of the westward electrojet during magnetically disturbed periods, *Journal of Geophysical Research: Space Physics*, *110*(A1).

Akasofu, S.-I. (1964), The development of the auroral substorm, *Planetary and Space Science*, *12*(4), 273–282.

Baker, K., R. Greenwald, J. Villian, and S. Wing (1988), Spectral characteristics of high frequency (hf) backscatter for high latitude ionospheric irregularities: Preliminary analysis of statistical properties, *Tech. rep.*, JOHNS HOPKINS UNIV LAUREL MD APPLIED PHYSICS LAB.

Baker, K., J. Dudeney, R. Greenwald, M. Pinnock, P. Newell, A. Rodger, N. Mattin, and C.-I. Meng (1995), Hf radar signatures of the cusp and low-latitude boundary layer, *Journal of Geophysical Research: Space Physics*, *100*(A5), 7671–7695.

Bates, H. F., and P. R. Albee (1970), Aspect sensitivity of f-layer hf backscatter echoes, *Journal of Geophysical Research*, *75*(1), 165–170.

Baumjohann, W., and R. A. Treumann (2012), *Basic space plasma physics*, Imperial College Press.

Beynon, W. (1975), Marconi, radio waves, and the ionosphere, *Radio Science*, *10*(7), 657–664.

Birkeland, K. (1908), *The Norwegian aurora polaris expedition 1902-1903*, vol. 1, H. Aschehoug & Company.

Bland, E. (2012), Real-Time Determination of foF2 using SuperDARN Interferometry, Bsc thesis, La Trobe University.

Bland, E. C., A. J. McDonald, S. de Larquier, and J. C. Devlin (2014), Determination of ionospheric parameters in real time using superdarn hf radars, *Journal of Geophysical Research: Space Physics*, *119*(7), 5830–5846.

Bland, E. C., E. Heino, M. J. Kosch, and N. Partamies (2018), Superdarn radar-derived hf radio attenuation during the september 2017 solar proton events, *Space Weather*, *16*(10), 1455–1469.

Chapman, S., and V. C. Ferraro (1931), A new theory of magnetic storms, *Terrestrial Magnetism and Atmospheric Electricity*, *36*(2), 77–97.

Chen, X.-C., D. Lorentzen, J. Moen, K. Oksavik, L. Baddeley, and M. Lester (2016), F region ionosphere effects on the mapping accuracy of superdarn hf radar echoes, *Radio Science*, *51*(5), 490–506.

Chisham, G., and M. Freeman (2003), A technique for accurately determining the cusp-region polar cap boundary using superdarn hf radar measurements, in *Annales Geophysicae*, vol. 21, pp. 983–996.

Chisham, G., and M. Freeman (2004), An investigation of latitudinal transitions in the superdarn doppler spectral width parameter at different magnetic local times, in *Annales Geophysicae*, vol. 22, pp. 1187–1202.

Chisham, G., M. Lester, S. E. Milan, M. Freeman, W. Bristow, A. Grocott, K. McWilliams, J. Ruohoniemi, T. K. Yeoman, P. L. Dyson, et al. (2007), A decade of the super dual auroral radar network (superdarn): Scientific achievements, new techniques and future directions, *Surveys in geophysics*, *28*(1), 33–109.

Chisham, G., T. K. Yeoman, and G. Sofko (2008), Mapping ionospheric backscatter measured by the superdarn hf radars–part 1: A new empirical

virtual height model, in *Annales Geophysicae*, vol. 26, pp. 823–841, Copernicus GmbH.

Cole, K. (1963), Some general theory of electron density irregularities in the ionospheric e-region, *Planetary and Space Science*, *11*, 759–765.

Coleman, C. (1998), A ray tracing formulation and its application to some problems in over-the-horizon radar, *Radio Science*, *33*(4), 1187–1197.

Dungey, J. W. (1961), Interplanetary magnetic field and the auroral zones, *Physical Review Letters*, *6*(2), 47.

Feldman, U., E. Landi, and N. Schwadron (2005), On the sources of fast and slow solar wind, *Journal of Geophysical Research: Space Physics*, *110*(A7).

Forsyth, C., I. Rae, J. Coxon, M. Freeman, C. Jackman, J. Gjerloev, and A. Fazakerley (2015), A new technique for determining substorm onsets and phases from indices of the electrojet (sophie), *Journal of Geophysical Research: Space Physics*, *120*(12), 10–592.

Gillies, R., G. Hussey, G. Sofko, K. McWilliams, R. Fiori, P. Ponomarenko, and J.-P. St.-Maurice (2009), Improvement of superdarn velocity measurements by estimating the index of refraction in the scattering region using interferometry, *Journal of Geophysical Research: Space Physics*, *114*(A7).

Greenwald, R., K. Baker, R. Hutchins, and C. Hanuise (1985), An hf phased-array radar for studying small-scale structure in the high-latitude ionosphere, *Radio Science*, *20*(1), 63–79.

Greenwald, R., K. Baker, J. Dudeney, M. Pinnock, T. Jones, E. Thomas, J.-P. Villain, J.-C. Cerisier, C. Senior, C. Hanuise, et al. (1995), Darn/superdarn, *Space Science Reviews*, *71*(1-4), 761–796.

Hapgood, M. (1992), Space physics coordinate transformations: A user guide, *Planetary and Space Science*, *40*(5), 711–717.

Hargreaves, J. K. (1992), *The solar-terrestrial environment: an introduction to geospace-the science of the terrestrial upper atmosphere, ionosphere, and magnetosphere*, Cambridge University Press.

Heikkila, W. J., and J. Winningham (1971), Penetration of magnetosheath plasma to low altitudes through the dayside magnetospheric cusps, *Journal of Geophysical Research*, *76*(4), 883–891.

Hosokawa, K., K. Shiokawa, Y. Otsuka, A. Nakajima, T. Ogawa, and J. Kelly (2006), Estimating drift velocity of polar cap patches with all-sky airglow imager at Resolute Bay, Canada, *Geophysical research letters*, *33*(15).

Hunsucker, R. D., and J. K. Hargreaves (2007), *The high-latitude ionosphere and its effects on radio propagation*, Cambridge University Press.

Johnsen, M. G. (2013), Real-time determination and monitoring of the auroral electrojet boundaries, *Journal of Space Weather and Space Climate*, *3*, A28.

Kallenrode, M.-B. (2013), *Space physics: an introduction to plasmas and particles in the heliosphere and magnetospheres*, Springer Science & Business Media.

Kelley, M. C. (2009), *The Earth's ionosphere: plasma physics and electrodynamics*, vol. 96, Academic press.

Kivelson, A. (1995), *Introduction to space physics*, Cambridge University Press.

Koskinen, H. (2011), *Physics of space storms: From the solar surface to the Earth*, Springer Science & Business Media.

Koustov, A., P. Ponomarenko, C. Graf, R. Gillies, and D. Themens (2018), Optimal f region electron density for the polardarn radar echo detection near the resolute bay zenith, *Radio Science*, *53*(9), 1002–1013.

Liu, L., W. Wan, Y. Chen, and H. Le (2011), Solar activity effects of the ionosphere: A brief review, *Chinese Science Bulletin*, *56*(12), 1202–1211.

Lowder, C., J. Qiu, and R. Leamon (2017), Coronal holes and open magnetic flux over cycles 23 and 24, *Solar Physics*, *292*(1), 18.

Lyons, L., Y. Nishimura, E. Donovan, and V. Angelopoulos (2013), Distinction between auroral substorm onset and traditional ground magnetic onset signatures, *Journal of Geophysical Research: Space Physics*, *118*(7), 4080–4092.

McDonald, A. J., J. Whittington, S. de Larquier, E. Custovic, T. A. Kane, and J. C. Devlin (2013), Elevation angle-of-arrival determination for a standard and a modified superdarn hf radar layout, *Radio Science*, *48*(6), 709–721.

McPherron, R. L. (1970), Growth phase of magnetospheric substorms, *Journal of Geophysical Research*, *75*(28), 5592–5599.

McWilliams, K., D. Andre, R. Greenwald, A. Schiffler, G. Sofko, and T. Yeoman (2003), Superdarn pulse sequences optimization and testing, in *2003 SuperDARN workshop*, Finland, doi:https://www.newcastle.edu.au/__data/assets/pdf_file/0006/57048/FITACF-Tutorial.pdf.

Milan, S., T. Jones, T. Robinson, E. Thomas, and T. Yeoman (1997), Interferometric evidence for the observation of ground backscatter originating behind the cutlass coherent hf radars, in *Annales Geophysicae*, vol. 15, pp. 29–39, Springer.

Milan, S., M. Lester, T. Yeoman, T. R. Robinson, M. Uspensky, and J.-P. Villain (2004), HF radar observations of high-aspect angle backscatter from the E-region, *Ann. Geophys.*, *22*, doi:10.5194/angeo-22-829-2004.

Nagai, T., D. Baker, and P. Higbie (1983), Development of substorm activity in multiple-onset substorms at synchronous orbit, *Journal of Geophysical Research: Space Physics*, *88*(A9), 6994–7004.

Newell, P. T., and C.-I. Meng (1992), Mapping the dayside ionosphere to the magnetosphere according to particle precipitation characteristics, *Geophysical Research Letters*, *19*(6), 609–612.

Ogilvie, K., and M. Coplan (1995), Solar wind composition, *Reviews of geophysics*, *33*(S1), 615–622.

Oksavik, K., J. Ruohoniemi, R. Greenwald, J. Baker, J. Moen, H. Carlson, T. K. Yeoman, and M. Lester (2006), Observations of isolated polar cap patches by the european incoherent scatter (eiscat) svalbard and super dual auroral radar network (superdarn) finland radars, *Journal of Geophysical Research: Space Physics*, *111*(A5).

Partamies, N., L. Juusola, E. Tanskanen, K. Kauristie, J. Weygand, and Y. Ogawa (2011), Substorms during different storm phases, *29*(11), 2031–2043.

Pfaff, R. F. (2012), The near-earth plasma environment, *Space science reviews*, *168*(1-4), 23–112.

Pitout, F., C. Escoubet, B. Klecker, and H. Rème (2006), Cluster survey of the mid-altitude cusp: 1. size, location, and dynamics, in *Annales Geophysicae*, vol. 24, pp. 3011–3026.

Ponomarenko, P., J. St-Maurice, C. Waters, R. Gillies, and A. Koustov (2009), Refractive index effects on the scatter volume location and doppler velocity estimates of ionospheric hf backscatter echoes, in *Annales geophysicae: atmospheres, hydrospheres and space sciences*, vol. 27, p. 4207.

Ruohoniemi, J., and R. Greenwald (1995), Observations of imf and seasonal effects in high-latitude convection, *Geophysical research letters*, *22*(9), 1121–1124.

Ruohoniemi, J., and R. Greenwald (2005), Dependencies of high-latitude plasma convection: Consideration of interplanetary magnetic field, seasonal, and universal time factors in statistical patterns, *Journal of Geophysical Research: Space Physics*, *110*(A9).

Ruohoniemi, J., R. Greenwald, K. Baker, J.-P. Villain, C. Hanuise, and J. Kelly (1989), Mapping high-latitude plasma convection with coherent hf radars, *Journal of Geophysical Research: Space Physics*, *94*(A10), 13,463–13,477.

Russell, C. T. (1972), The configuration of the magnetosphere, in *Critical problems of magnetospheric physics*, p. 1.

Russell, C. T. (2000), The polar cusp, *Advances in Space Research*, *25*(7-8), 1413–1424.

Sandahl, I. (2003), The cusp as a source of plasma for the magnetosphere, *Advances in Space Research*, *31*(5), 1195–1205.

Schwenn, R. (2001), Solar wind: Global properties, *Encyclopedia of Astronomy and Astrophysics (Nature Publishing Group, Bristol, 2001)*.

Shi, J., J. Guo, M. Dunlop, T. Zhang, Z. Liu, E. Lucek, A. Fazakerley, H. Reme, and I. Dandouras (2012), Inter-hemispheric asymmetry of dependence of the cusp location on dipole tilt during northward imf conditions, *Annales Geophysicae*, *30*(1), 21–26.

SuperDARN Data Analysis Working Group (2018), SuperDARN Radar Software Toolkit (RST) (version 4.2), `https://doi.org/10.5281/zenodo.1143675`, participating members: Thomas, E. G. and Ponomarenko, P. V. and Billett, D. D. and Bland, E. C. and Burrell, A. G. and Kotyk, K. and Reimer, A. S. and Schmidt, M. and Shepherd, S. G. and Sterne, K. T. and Walach, M.-T.

Tanskanen, E., T. I. Pulkkinen, A. Viljanen, K. Mursula, N. Partamies, and J. Slavin (2011), From space weather toward space climate time scales: Substorm analysis from 1993 to 2008, *Journal of Geophysical Research: Space Physics*, *116*(A5).

Tolmacheva, A. (1970), The contribution of cosmic rays to the ionization of the d-region of the ionosphere, *Radiophysics and Quantum Electronics*, *13*(6), 655–660.

Velinov, P., A. Mishev, and L. Mateev (2009), Model for induced ionization by galactic cosmic rays in the earth atmosphere and ionosphere, *Advances in Space Research*, *44*(9), 1002–1007.

Villain, J., R. Greenwald, and J. Vickrey (1984), Hf ray tracing at high latitudes using measured meridional electron density distributions, *Radio Science*, *19*(1), 359–374.

Wing, S., P. Newell, and C.-I. Meng (2005), Cusp modeling and observations at low altitude, in *The Magnetospheric Cusps: Structure and Dynamics*, pp. 341–367, Springer.

Yermolaev, Y. I., and M. Y. Yermolaev (2010), Solar and interplanetary sources of geomagnetic storms: Space weather aspects, *Izvestiya, Atmospheric and Oceanic Physics*, *46*(7), 799–819.

Zell, H. (2015), X Marks the Spot for Magnetic Reconnection, doi:https://www.nasa.gov/content/goddard/x-marks-spot-for-magnetic-reconnection.

Zurbuchen, T., L. Fisk, G. Gloeckler, and R. Von Steiger (2002), The solar wind composition throughout the solar cycle: A continuum of dynamic states, *Geophysical research letters*, *29*(9), 66–1.

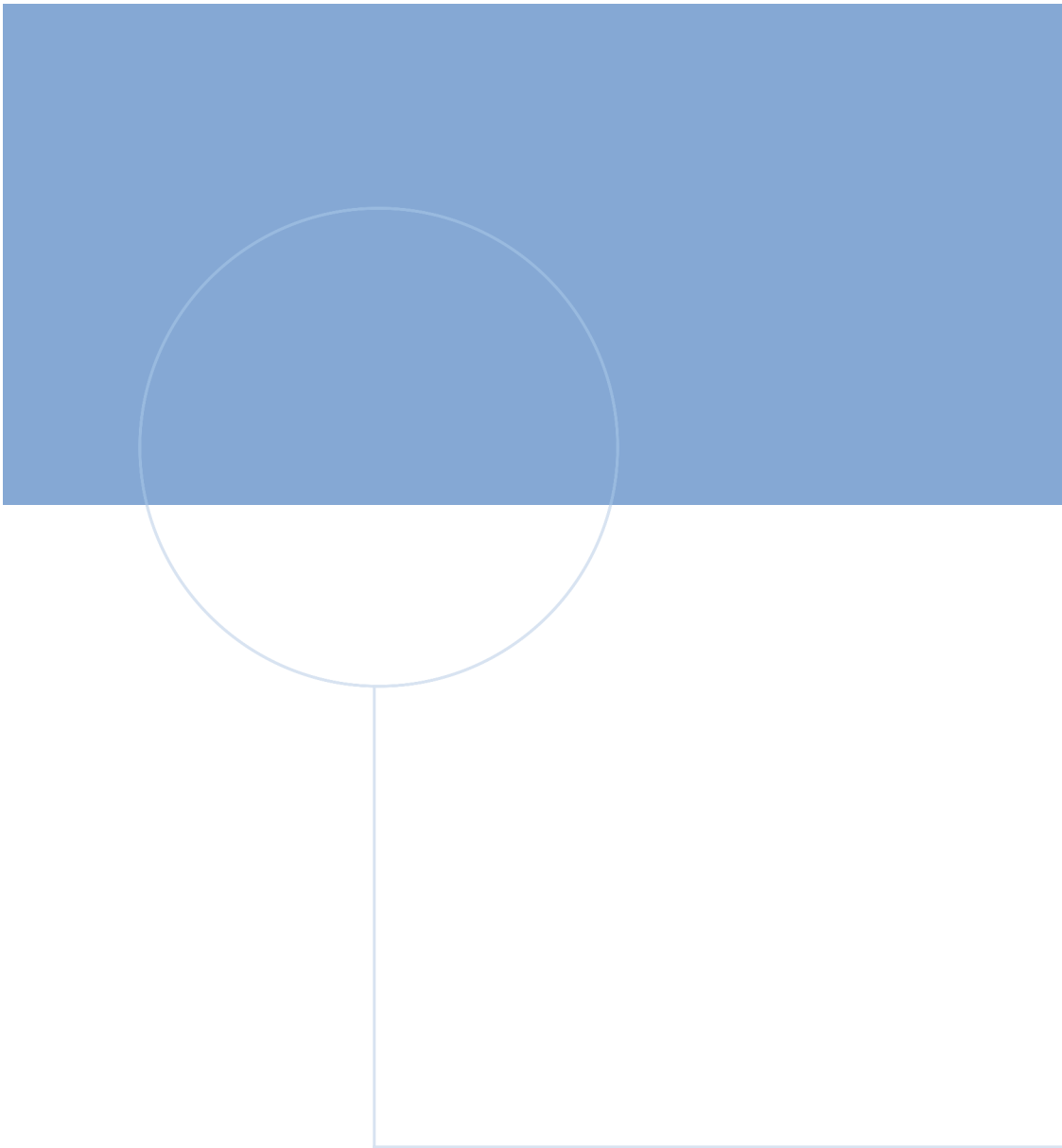

NTNU
Norwegian University of
Science and Technology